JAMES | Journal of Advances in Modeling Earth Systems

RESEARCH ARTICLE
10.1029/2022MS003465

Application of Satellite-Based Detections of Arctic Bromine Explosion Events Within GEOS-Chem

P. A. Wales[1,2,3], C. A. Keller[1,3,4], K. E. Knowland[1,3,4], S. Pawson[1], S. Choi[5,6], F. Hendrick[7], M. Van Roozendael[7], R. J. Salawitch[8,9], R. Sulieman[10], and W. F. Swanson[11]

[1]Global Modeling and Assimilation Office, NASA Goddard Space Flight Center, Greenbelt, MD, USA, [2]NASA Postdoctoral Program, Universities Space Research Association, Columbia, MD, USA, [3]Now at Goddard Earth Sciences Technology & Research II, Morgan State University, Baltimore, MD, USA, [4]Goddard Earth Science Technology & Research, Universities Space Research, Association, Columbia, MD, USA, [5]Atmospheric Chemistry and Dynamics Laboratory, NASA Goddard Space Flight Center, Greenbelt, MD, USA, [6]Science Systems and Applications, Inc., Lanham, MD, USA, [7]Royal Belgian Institute for Space Aeronomy (BIRA-IASB), Brussels, Belgium, [8]Department of Atmospheric and Oceanic Sciences, University of Maryland, College Park, MD, USA, [9]Earth System Science Interdisciplinary Center, University of Maryland, College Park, MD, USA, [10]Harvard-Smithsonian Center for Astrophysics, Cambridge, MA, USA, [11]Department of Chemistry and Biochemistry and Geophysical Institute, University of Alaska Fairbanks, Fairbanks, AK, USA

Abstract During polar spring, periods of elevated tropospheric bromine drive near complete removal of surface ozone. These events impact the tropospheric oxidative capacity and are an area of active research with multiple approaches for representing the underlying processes in global models. We present a method for parameterizing emissions of molecular bromine (Br_2) over the Arctic using satellite retrievals of bromine monoxide (BrO) from the Ozone Monitoring Instrument (OMI). OMI retrieves column BrO with daily near global coverage, and we use the GEOS-Chem chemical mechanism, run online within the Goddard Earth Observing System Earth System Model to identify hotspots of BrO likely associated with polar processes. To account for uncertainties in modeling background BrO, hotspots are only identified where the difference between OMI and modeled columns exceeds a statistical threshold. The resulting hotspot columns are a lower-limit for the portion of OMI BrO attributable to bromine explosion events. While these hotspots are correlated with BrO measured in the lower troposphere over the Arctic Ocean, a case study of missing detections of near-surface BrO is identified. Daily flux of Br_2 is estimated from hotspot columns of BrO using internal model parameters. When the emissions are applied, BrO hotspots are modeled with a 5% low bias. The sensitivity of the resulting ozone simulations to the treatment of background uncertainties in the BrO column is demonstrated. While periods of isolated, large (>50%) decreases in surface ozone are modeled, this technique does not simulate the low ozone observed at coastal stations and consistently underestimates ozone loss during March.

Plain Language Summary During polar spring, high levels of bromine-containing molecules drive near complete removal of surface ozone (O_3), impacting the chemistry of the troposphere and the biological uptake of mercury. Global models currently have multiple mechanisms for representing the underlying processes that produce brominated molecules in polar regions. We estimate molecular bromine (Br_2) emissions from measurements of bromine monoxide (BrO) collected over the Arctic by a satellite instrument. An atmospheric model, run without polar emissions of Br_2, is used to estimate how much of the satellite BrO signal is due to background processes in the stratosphere and troposphere and isolate the portion of the signal likely associated with Arctic emissions. We account for uncertainties in the model representation of background BrO using a statistical threshold. Because of the catalytic nature of bromine-mediated ozone depletion, we focus our initial efforts on developing a lower-limit estimate of Arctic emissions. The amount of BrO attributed to polar processes and the resulting impact on O_3 are sensitive to the magnitude of the statistical threshold, with a better representation of surface O_3 achieved with a lower threshold. While the satellite-based emissions result in periodic decreases in surface O_3 in late spring, modeled O_3 is consistently high with respect to observations, particularly during early spring.

Key Points:

- BrO hotspots are isolated from satellite signals using modeled columns of BrO and a bias threshold to account for model uncertainties
- We estimate Arctic Br_2 emissions from BrO signals and demonstrate the sensitivity of modeled O_3 to the BrO hotspot detection threshold
- Simulations with satellite-based Br_2 emissions overestimate springtime Arctic surface O_3 with few ozone depleting events modeled in March

Supporting Information:

Supporting Information may be found in the online version of this article.

Correspondence to:

P. A. Wales,
pamela.a.wales@nasa.gov

Citation:

Wales, P. A., Keller, C. A., Knowland, K. E., Pawson, S., Choi, S., Hendrick, F., et al. (2023). Application of satellite-based detections of Arctic bromine explosion events within GEOS-Chem. *Journal of Advances in Modeling Earth Systems*, *15*, e2022MS003465. https://doi.org/10.1029/2022MS003465

Received 14 OCT 2022
Accepted 11 JUL 2023

1. Introduction

During polar spring, elevated levels of tropospheric brominated species, referred to as "bromine explosion events," have been detected over both the Arctic and Antarctic (e.g., Barrie et al., 1988; Frieß et al., 2004; Oltmans et al., 1989; Richter et al., 1998). These bromine explosions drive boundary layer ozone depletion events (ODEs), where ozone (O_3) rapidly decreases from background mixing ratios to levels near zero (e.g., Bottenheim & Chan, 2006; Halfacre et al., 2014; Jones et al., 2006; Wessel et al., 1998). During ODEs, halogens become the main tropospheric oxidant, impacting the lifetimes of Arctic pollutants (Bloss et al., 2010; Evans et al., 2003) and increasing the deposition and biological uptake of oxidized mercury (Gao et al., 2022; Holmes et al., 2006; Schroeder et al., 1998; Stephens et al., 2012; S. Wang et al., 2019a). The underlying process resulting in bromine explosion events is connected to sea ice and thus is susceptible to the influence of climate change in polar regions (Pratt, 2019). However, there are currently multiple approaches for representing bromine explosion events in global models.

Similar to reactions that occur in the stratosphere, O_3 loss catalyzed by brominated species in the troposphere occurs via reactions between atomic bromine (Br) and bromine monoxide (BrO):

$$Br + O_3 \rightarrow BrO + O_2 \quad (1)$$

$$BrO + BrO \rightarrow 2Br + O_2 \quad (2)$$

Through gaseous and heterogeneous reactions, the brominated radicals cycle among the family of inorganic bromine compounds (e.g., Finlayson-Pitts, 2010; Saiz-Lopez & von Glasow, 2012; Simpson et al., 2015). This family, termed Br_y, includes the sum of all inorganic gas phase species, multiplied by bromine atomicity (BrO + Br + 2 × Br_2 + BrCl + BrI + $BrNO_3$ + $BrNO_2$ + HBr + HOBr). Chlorine (Custard et al., 2017; Foster et al., 2001; Keil & Shepson, 2006; Liao et al., 2014) and iodine (Mahajan et al., 2010; Raso et al., 2017) containing compounds have been observed during polar spring. Historically, detection of iodine over the Arctic has been inconsistent (Saiz-Lopez et al., 2012), but a recent ship-borne campaign has reported enhanced iodine monoxide mixing ratios over the Arctic Ocean (Benavent et al., 2022). While both halogen species increase the catalytic efficiency of bromine-mediated ozone loss, chlorine is less efficient at depleting O_3 due to competing reactivity with methane and hydrocarbons (Thompson et al., 2015).

Bromine explosion events are supplied by aqueous (aq) bromide ions (Br^-) from sea salt and converted into gas phase brominated species through heterogeneous reaction on polar surfaces (e.g., saline snow and aerosol particles). Hypobromous acid (HOBr), formed from BrO:

$$BrO + HO_2 \rightarrow HOBr + O_2 \quad (3)$$

converts Br^- (aq) into gaseous molecular bromine (Br_2):

$$HOBr + Br^-(aq) + H^+(aq) \rightarrow H_2O + Br_2 \quad (4)$$

The produced Br_2 rapidly photolyzes to reform Br:

$$Br_2 + h\upsilon \rightarrow 2Br \quad (5)$$

which feeds back into Br_y and the formation of HOBr (reactions 1–3). Reaction 4 is considered to be the main pathway for bromine explosion events, and multiple saline surfaces have been considered for this heterogeneous process (Fan & Jacob, 1992; Simpson et al., 2007; Wennberg, 1999).

The surfaces considered include saline snowpacks over sea ice and land (Cao et al., 2014; Foster et al., 2001; Pratt et al., 2013) and sea salt aerosols generated by wind-driven blowing snow (Frey et al., 2020; Huang et al., 2018), with multiple studies reporting direct observations of Br_2 above snowpacks (e.g., Custard et al., 2017; Pratt et al., 2013; Raso et al., 2017). The saline surfaces used to model the release of Br_2 are typically continental and sea ice snowpacks (Falk & Sinnhuber, 2018; Fernandez et al., 2019; Herrmann et al., 2021; Toyota et al., 2011) or sea salt aerosols from blowing snow (Huang et al., 2020; Yang et al., 2005, 2010; Zhao et al., 2016), and two recent modeling efforts have also represented bromine explosion events using a combination of snowpack and blowing snow source mechanisms (Marelle et al., 2021; Swanson et al., 2022). In both mechanisms, the Br^- in sea water is frozen in sea ice and taken up by the snowpack or deposited by aerosols and trace gases (Domine et al., 2004).

However, blowing snow processes occur under high wind conditions, while snowpack related processes are typically associated with low wind and a stable boundary layer (Jones et al., 2009; Peterson et al., 2015; Swanson et al., 2020). While Marelle et al. (2021) found that brominated compounds emitted by blowing snow had a minor impact on surface O_3 simulations relative to snowpack, other studies have been able to capture ODEs using only blowing snow sources (Huang et al., 2020; Yang et al., 2010). Furthermore, Yang et al. (2020) demonstrated that two models using similar bromine emissions schemes produced dissimilar Br_y and O_3 fields, with neither model capturing both the tropospheric background and hotspot columns of BrO, reflecting the sensitivity of these simulations to differences in the modeled partitioning and resulting deposition of Br_y species.

In the present study, we parameterize emission estimates of Br_2 over the Arctic based on retrievals of BrO from the Ozone Monitoring Instrument (OMI) onboard NASA's Aura satellite. Levels of Br_y can be inferred from observations of BrO, and modeling studies frequently use satellite-based tropospheric columns of BrO to assess the performance of bromine explosion simulations (Herrmann et al., 2021; Huang et al., 2020; Toyota et al., 2011; Yang et al., 2010; Zhao et al., 2016). Satellite-based studies have frequently associated elevated BrO events with blowing snow conditions (Begoin et al., 2010; Blechschmidt et al., 2016; Choi et al., 2018), but ground-based studies have proposed that the BrO enhancements under shallow boundary layer conditions may not be detectable from space-based instruments (Sihler et al., 2012). Enhanced vertical columns of BrO associated with bromine explosion events were first detected by the Global Ozone Monitoring Experiment satellite instrument (Chance, 1998; Richter et al., 1998; Wagner & Platt, 1998). In present day, multiple satellite instruments provide column retrievals of BrO with daily, global coverage (Seo et al., 2019; Sihler et al., 2012; Suleiman et al., 2019; Theys et al., 2011). The long-term record of BrO column retrievals has been used to connect increasing amounts of Arctic BrO to the increasing relative amount of first-year to multiyear sea ice (Bougoudis et al., 2020; Hollwedel et al., 2004) and have been used to train an artificial neural network representation of tropospheric columns (Bougoudis et al., 2022).

We interpret OMI retrievals of BrO using the GEOS-Chem chemical mechanism, coupled to the NASA Goddard Earth Observing System (GEOS) Earth system model. Section 2 provides a description of the employed model setup and instrumental measurements. The model setup was designed to be similar to the near-real time GEOS Composition Forecast (GEOS-CF, v1.0; Keller et al., 2021) system to facilitate the application of the results of this study in future efforts within the Global Modeling and Assimilation Office. Additionally, Huang et al. (2020) and Swanson et al. (2022) have developed mechanisms for blowing snow and snowpack sources of bromine explosion events for the GEOS-Chem code, allowing for the availability of different approaches for representing polar emissions of brominated species within one chemical mechanism. Ground-based retrievals of BrO retrieved over Harestua, Norway are used to assess the vertical distribution of BrO in base model runs, while the performance of simulations with an Arctic source of Br_2 is evaluated using measurements of BrO and O_3 collected by instruments onboard ice-tethered buoys and measurements of O_3 from coastal monitoring stations.

In Section 3.1, we describe how the model is used to isolate tropospheric hotspots of BrO from OMI column retrievals over the Arctic with a threshold approach similar to past satellite-based studies (Bougoudis et al., 2020; Choi et al., 2018; Hollwedel et al., 2004; Seo et al., 2020; Theys et al., 2011). Due to the catalytic nature of these emissions, our preliminary efforts are focused on developing a lower-limit estimate. In Section 3.2, we estimate the associated Br_2 flux that needs to be included to simulate the tropospheric hotspots. These fluxes are implemented in the model where elevated BrO signals are detected, agnostic of proximity to sea ice or continental tundra. The resulting simulations are evaluated with respect to observations of BrO, and the impact of the added Br_y on surface O_3 simulations is assessed in Section 3.3. Conclusions are provided in Section 4.

2. Model and Measurement Descriptions

2.1. Model Setup

In this study, version 12.0.1 of the GEOS-Chem chemical mechanism was run as a chemical module coupled to the NASA GEOS Earth system model (Hu et al., 2018; Long et al., 2015). Stratospheric updates to the version 12.0.1 chemical mechanism are applied as they were described for the GEOS-CF system (Knowland et al., 2022). The GEOS earth system model coupled chemistry framework (Nielsen et al., 2017) allows for the different chemical and aerosol mechanisms to be coupled to the GEOS atmospheric general circulation model (AGCM; Molod et al., 2015). Dynamical fields are determined online by the GEOS AGCM and are constrained to meteorological

fields from the Modern-Era Retrospective Analysis for Research and Applications version 2 (MERRA-2) reanalysis (Gelaro et al., 2017) in "replay" mode (Orbe et al., 2017). All simulations were performed at a cubed sphere c90 horizontal resolution (nominally, 1° latitude × 1.25° longitude) with 72 levels from the surface layer up to 0.01 hPa. A description of the coupling between GEOS AGCM and GEOS-Chem is given in Keller et al. (2021) and Figure S1 of Knowland et al. (2022). While the physics computed within the GEOS AGCM use MERRA-2 reanalysis O_3, in the present model setup, ozone fields within the GEOS-Chem chemical module are free-running and calculated by the chemical mechanism. The use of free-running O_3 fields facilitates comparisons between modeled and OMI retrieved column O_3 to assess the performance of the stratospheric mechanism over the Arctic during boreal spring (Section 3.1).

The GEOS-Chem mechanism employs a detailed representation of HO_x-NO_x-VOC-ozone-halogen-aerosol chemistry (Bey et al., 2001). The halogen mechanism in GEOS-Chem v12.0.1 includes interactive chlorine, bromine, and iodine chemistry with gas phase and heterogeneous reactions (Sherwen et al., 2016b). In version 12.0.1 of the mechanism, iodine is supplied by marine emissions of organic and inorganic compounds (Sherwen et al., 2016a), and chlorine is supplied by anthropogenic and oceanic processes (Eastham et al., 2014; Schmidt et al., 2016), neither of which include polar specific sources. The bromine chemical mechanism, with aerosol uptake coefficients and heterogeneous recycling, is described by Schmidt et al. (2016) for the troposphere and by Eastham et al. (2014) for the stratosphere. Chen et al. (2017) introduced the reaction between HOBr and dissolved SO_2 (S(IV)=HSO_3^- + SO_3^{2-}) on cloud droplets that reduces the tropospheric loading of Br_y. Following Schmidt et al. (2016), the bromine source from sea salt aerosols was not included in our simulations, since this source results in unrealistically high BrO in the marine boundary layer. Thus, the sources of tropospheric Br_y in our base simulation is from photodecomposition of organic brominated species and transport from the stratosphere.

Simulations were conducted with the fully coupled tropospheric and stratospheric chemical mechanism (Eastham et al., 2014) with the revisions described by Knowland et al. (2022). Briefly, the updates to the GEOS-Chem mechanism applied here include: kinetic rate constants and photolysis cross sections follow the recommendations from the 2015 Jet Propulsion Lab kinetic evaluation (Burkholder et al., 2015), and surface boundary conditions for ozone depleting substances are defined by the World Meteorological Organization 2018 baseline scenario (Carpenter et al., 2018). Family transport of Br_y and inorganic chlorine species has been implemented to eliminate spurious maxima in the inorganic halogen families (e.g., Douglass et al., 2004). Additionally, in accordance with the Global Modeling Initiative chemical mechanism (Douglass et al., 2004; Strahan et al., 2007), three heterogeneous reactions that produce BrCl have been turned off for stratospheric aerosols (Knowland et al., 2022). While simulations of BrO were not specifically evaluated in past GEOS-Chem studies with stratospheric chemistry, the stratospheric loading of brominated species was determined in Knowland et al. (2022) to be in agreement with the recommended values provided by Engel et al. (2018).

Our base simulation, presented in Section 3, was run for January 2008 through December 2012. The model was spun-up as a free-running system for 9 years, starting in 1999, as described in Section 4 of Knowland et al. (2022). This spin-up was found to produce realistic latitudinal and vertical distributions of chlorine and nitrogen containing trace gases with respect to profile retrievals collected by satellite instruments (Knowland et al., 2022). The final spin-up year was replayed to MERRA-2 meteorology in order to have realistic atmospheric composition distributions for the specific years of interest. Two additional simulations are conducted with Arctic Br_2 emissions (Section 3.3), where surface emissions of Br_2 are added using the Harmonized Emissions Component (HEMCO; Keller et al., 2014).

2.2. Ozone Monitoring Instrument (OMI)

We use OMI retrievals to detect Arctic BrO signals associated with bromine explosion events. OMI is an ultraviolet (UV)-visible, nadir viewing spectrometer onboard the NASA Aura satellite (Levelt et al., 2006). The Aura satellite was launched in July 2004 in a sun-synchronous, polar orbit with an equatorial crossing time of 13:45 in the ascending node. The OMI swath width is 2,600 km with a 13 × 24 km^2 spatial resolution at the center of the swath. Beginning in June 2007, a partial blockage impacts radiances collected by specific detector rows, referred to as the row anomaly (Schenkeveld et al., 2017).

The primary OMI product used in this study is the version 3.0.5 retrieval of BrO (Chance, 2007; Suleiman et al., 2019). This retrieval uses a wavelength fitting window of 319–347.5 nm and BrO cross sections measured at

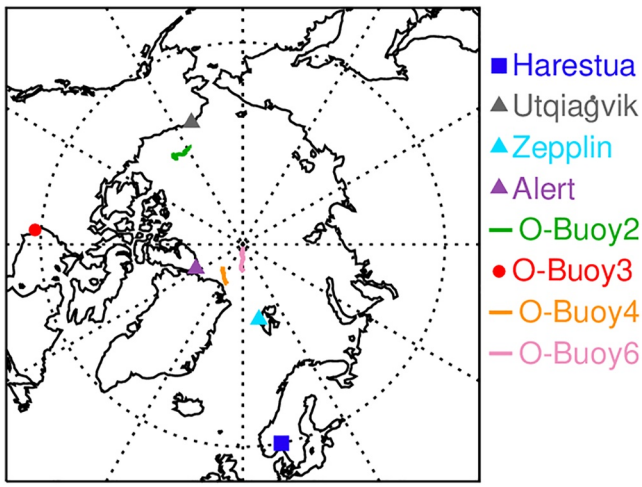

Figure 1. Locations of Harestua (Norway), Utqiaġvik (Alaska, USA), Zeppelin (Svalbard, Norway), and Alert (Nunavut, Canada) measurement stations, and of the O-Buoy deployments. Dotted lines every 30° longitude and a dotted circle indicates 60°N.

228 K by Wilmouth et al. (1999). Vertical column densities (VCD) of BrO are determined from observed slant path through the atmosphere using a wavelength and albedo dependent air mass factor (AMF) that is calculated prior to spectral fitting. Slant column densities (SCD) and VCDs of BrO are calculated following spectral fitting of BrO, Ring scattering, O_3, nitrogen dioxide (NO_2), formaldehyde (CH_2O), chlorine dioxide (OClO), and sulfur dioxide (SO_2). Additional OMI data included in our analysis are stratospheric column NO_2 from the NASA column NO_2 product (OMNO2; Bucsela et al., 2013; Krotkov et al., 2017), cloud pressure from the rotational Raman scattering product (OMCLDRR; Vasilkov et al., 2008), and total column ozone and surface reflectivity at 331 nm from the NASA product based on the total ozone mapping spectrometer algorithm (OMTO3; McPeters et al., 2008).

Traditionally, AMFs are used to account for scattering along the satellite-observed path through the atmosphere and convert SCDs of trace gases to VCDs:

$$\mathrm{VCD} = \frac{\mathrm{SCD}}{\mathrm{AMF}} \tag{6}$$

Since the OMI retrieval of BrO applies AMFs prior to spectral fitting, an effective AMF is provided from the ratio of OMI BrO SCD/VCD (AMF^{OMI}). This AMF uses a mostly stratospheric a priori profile of BrO, and the sensitivity of the OMI retrieval to the BrO signal is partially dependent on the profile shape of the absorbing trace gas with the satellite instrument generally less sensitive to BrO in the lower troposphere (Suleiman et al., 2019). Thus, when there are significant amounts of BrO in the lower troposphere, such as during bromine explosion events, the OMI retrieval will underestimate the VCD of BrO.

For our initial comparison to model output, OMI data from each Aura overpass is averaged within a 1° latitude × 1° longitude grid. Retrievals are filtered to remove observations affected by the row anomaly and collected at solar zenith angles (SZA) greater than 80°. AMFs are calculated from GEOS-Chem modeled profiles of BrO sampled at the OMI overpass time (AMF^{GC}) using scattering weight profiles prepared by Choi et al. (2012) with the Linearized Discrete Ordinate Radiative Transfer model (Spurr et al., 2001). Since mixing ratios of tropospheric BrO are relatively low in GEOS-Chem version 12.0.1 (shown in Section 3.1), the value of AMF^{GC} is similar to AMF^{OMI}, and the impact of differences in the OMI and modeled profiles of BrO on the analysis presented in Section 3.1 is negligible.

For analysis of tropospheric hotspots of BrO, where OMI underestimates the VCD of BrO, tropospheric AMF corrections are determined following Choi et al. (2018), described in Section 3.1. The application of the tropospheric correction requires additional filtering criteria such that retrievals are only included where the SZA < 80°, viewing zenith angle <65°, and OMI reflectivity at 331 nm >0.6. Regions influenced by optically thick clouds are removed where the difference between the surface and OMI detected cloud pressures are >100 hPa, as defined by the OMCLDRR product (Vasilkov et al., 2010).

2.3. Ground-Based Measurements of BrO Over Harestua

Modeled stratospheric and tropospheric columns of BrO are compared to ground-based retrievals over Harestua, Norway (60°N, 11°E; see Figure 1) collected using zenith-sky ultraviolet-visible absorption spectroscopy (Hendrick et al., 2007, 2009). The Harestua station is part of the Network of the Detection of Atmospheric Composition Change (NDACC). A complete description of the instrument setup and BrO retrieval algorithm is given by Hendrick et al. (2007) with updates described in Choi et al. (2018). Slant column densities of BrO are retrieved using the differential optical absorption spectroscopy (DOAS; U. Platt & Stutz, 2008) technique at twilight hours. The DOAS retrieval algorithm uses the 336–359 nm wavelength fitting window with BrO cross sections from Fleischmann et al. (2004) and includes spectral fitting of BrO, the Ring effect, O_3, NO_2, O_2–O_2 collision complex, and OClO.

The Harestua BrO columns shown in Section 3.1 were prepared in support of earlier OMI studies (Choi et al., 2018; Suleiman et al., 2019). Values of SCDs of BrO are collected at high SZAs (80°, 85°, and 90°).

Vertical profiles and VCDs of BrO are determined from the twilight measurements using the Optimal Estimation Method (OEM, Rodgers, 2000). Sunset profiles of BrO are converted to 13:30 local time using a stacked photochemical box model for comparison to the approximate OMI overpass time. This model also allows for the rapid variation of BrO in twilight hours to be accounted for in the radiative transfer simulations associated with the profile retrieval (Hendrick et al., 2007, 2009).

Hourly modeled output at 60°N, 11°E are interpolated over time to 13:30 local time for comparison to retrieved tropospheric and stratospheric columns collected between 2008 and 2011. In accordance with Hendrick et al. (2007), columns are filtered to only include observations collected between 15 February and 31 October each year, except for 2011 where separated tropospheric and stratospheric retrievals are only available through June. Errors associated with the ground-based VCDs, shown in Section 3.1, are calculated from the root sum of squares combination of the random and systematic errors.

2.4. Autonomous, Ice-Tethered Buoy Measurements

OMI-based detections of BrO hotspots and simulations with Arctic Br_2 emissions are evaluated using measurements of BrO and O_3 collected during four deployments of autonomous, ice-tethered buoys (O-Buoys) (Knepp et al., 2010). Data is publicly available through the National Science Foundation (NSF) Arctic Data Center (Simpson et al., 2009). Columns of BrO were retrieved from multi-axis differential optical absorption spectroscopy (MAX-DOAS) instruments (Carlson et al., 2010; Peterson et al., 2015), and surface mixing ratios of O_3 were measured by a UV-absorption sensor (Halfacre et al., 2014; Knepp et al., 2010). Springtime measurements of BrO were collected in 2011 by O-Buoys 2 and 3 and in 2012 by O-Buoys 4 and 6. Coincident observations of O_3 with BrO are available for O-Buoy 2 and 4 deployments, while coincident measurements are sparse during O-Buoy 3 and 6 deployments. The MAX-DOAS BrO retrievals were collected above the buoy tracks shown in Figure 1. Figure 1 also includes the locations of the Harestua (Section 2.3, shown as a square) and three coastal ozone stations (Section 2.5, shown as triangles).

The MAX-DOAS instrument collects profiles of BrO from the surface to 4 km through the optimal estimation procedure (Frieß et al., 2006; Peterson et al., 2015). Peterson et al. (2015) determined the MAX-DOAS measurements are most sensitive to BrO signals that originate in a near surface layer, between the surface and 200 m, and in an aloft layer, between 200 and 2,000 m. The sensitivity to a priori information is reduced if the retrieval is represented as columns of BrO in the lowest 200 m above the surface (BrO^{200m}) and in the lower troposphere (BrO^{LT}), between the surface and 2,000 m. The retrievals are filtered to only included data where the degrees of freedom for the signal in the near surface layer is >0.7 and in the aloft layer is >0.5 (Simpson et al., 2017). For comparison to OMI-based and simulated columns of BrO, only MAX-DOAS observations collected at SZAs < 80° are included in our study.

Hourly output of surface layer O_3 and profiles of BrO from GEOS-Chem simulations are sampled along the O-Buoy tracks at the closest time to each MAX-DOAS measurement. Columns of BrO^{200m} and BrO^{LT} are determined from modeled profiles of BrO following the method presented by Swanson et al. (2022). For each time step along the buoy track, partial columns of modeled BrO are calculated along the vertical resolution of the MAX-DOAS averaging kernels. The resulting profile of partial columns are scaled according using the mean averaging kernel sensitivity for BrO^{200m} and BrO^{LT}, where the averaging kernel sensitivities are near unity at the surface and less than 0.5 respectively above 200 and 2,000 m, as described by Swanson et al. (2022). Each set of scaled partial columns are summed from 0 to 4 km and averaged per day (SZA < 80°) to provide modeled BrO^{200m} and BrO^{LT}.

2.5. Station Ozone Measurements

Surface ozone simulations are evaluated using ground-level, in situ measurements collected at three coastal stations (see Figure 1) that detect springtime ODEs. Measurements from Utqiaġvik, Alaska, USA (71.3°N, 156.7°W) are available from the NOAA Global Monitoring Laboratory (McClure-Begley et al., 2014; Oltmans & Levy, 1994). The ozone record from the Zeppelin Observatory (78.9°N, 11.9°E) near Ny-Ålesund, Norway is provided by Norwegian Institute for Air Research (S. M. Platt et al., 2022; Tørseth et al., 2012). Lastly, measurements from Alert, Nunavut, Canada (82.5°N, 62.5°W) are available from the Canadian Air and Precipitation Monitoring Network (CAPMoN).

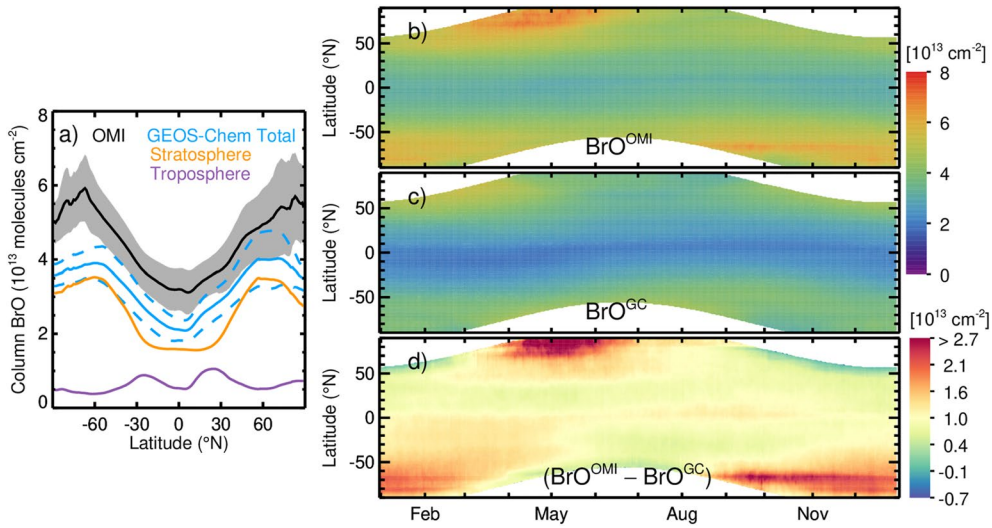

Figure 2. Ozone Monitoring Instrument (OMI) retrieved and GEOS-Chem simulated column BrO averaged over 2008–2012. (a) The black line and gray shaded region are the mean and standard deviation of OMI column BrO. The blue solid and dashed lines are the mean and standard deviation, respectively, of BrO^{GC} at OMI overpass time. The stratospheric and tropospheric components of the BrO^{GC} are shown as orange and purple lines, respectively. Daily, zonal mean (b) BrO^{OMI}, (c) BrO^{GC}, and (d) the difference between BrO^{OMI} and BrO^{GC} are shown averaged over 2008–2012.

3. Results and Discussion

A method for isolating OMI columns of BrO (hereafter, BrO^{OMI}) that are likely associated with Arctic bromine explosion events is presented in Section 3.1. A bias threshold is defined based on the difference between OMI and GEOS-Chem columns of BrO in non-polar regions (50°S to 50°N). Values of BrO^{OMI} larger than the bias threshold are identified as tropospheric hotspots of BrO (hereafter, BrO^{TH}) and represent a lower limit estimate for the magnitude of bromine explosion events. In Section 3.2, the process for estimating emissions of Br_2 from OMI-based BrO^{TH} and incorporating this flux into the model is described. In Section 3.3, simulations with Arctic Br_2 emissions are presented and are evaluated with respect to OMI and ice-tethered buoy observations of BrO. Additionally, the impact of the added emissions on modeled surface O_3 is presented, and the sensitivity of the simulations to the bias threshold is assessed.

3.1. Detecting Hotspots of BrO

Globally, the GEOS-Chem (v12.0.1) modeled BrO column (BrO^{GC}) is systematically biased low with respect to BrO^{OMI} (Figure 2). The black and blue solid lines in Figure 2a are the respective means of BrO^{OMI} and BrO^{GC} as a function of latitude, averaged over 2008–2012. The gray shading represents the standard deviation about the mean in BrO^{OMI}, while the blue dashed lines represent the standard deviation (σ) in BrO^{GC}. Daily, zonal averages of BrO^{OMI} and BrO^{GC} are shown in Figures 2b and 2c, respectively, with the difference between the two columns in Figure 2d. For all results presented in Section 3.1, hourly model output is interpolated to the OMI overpass times with BrO^{OMI} retrievals that pass filtering criteria. Preliminary comparisons of the total columns are filtered for the OMI row anomaly and for SZAs < 80° (Section 2.2).

Throughout the tropics and midlatitudes (50°S–50°N), the mean difference between BrO^{OMI} and BrO^{GC} is 1×10^{13} molecules cm^{-2}, with $\sigma = 0.6 \times 10^{13}$ molecules cm^{-2}. The majority of BrO^{GC} resides in the stratospheric column, as indicated by the orange line in Figure 2a. The larger values of BrO^{GC} simulated over northern high latitudes in Figure 2c are due to amplifications of the stratospheric column during boreal spring. During boreal summer months, the difference between BrO^{OMI} and BrO^{GC} over the Arctic is largely within the standard deviation of the bias at non-polar latitudes. However, larger differences between the columns are detected over the Arctic during boreal spring and along the Antarctic coast, as shown in red in Figure 2d.

We use ground-based observations over Harestua, Norway (61°N, 11°E) to evaluate the vertical distribution of GEOS-Chem columns of BrO at the closest grid-box to Harestua for 2008 through 2011 (Figure 3 and Figure S1

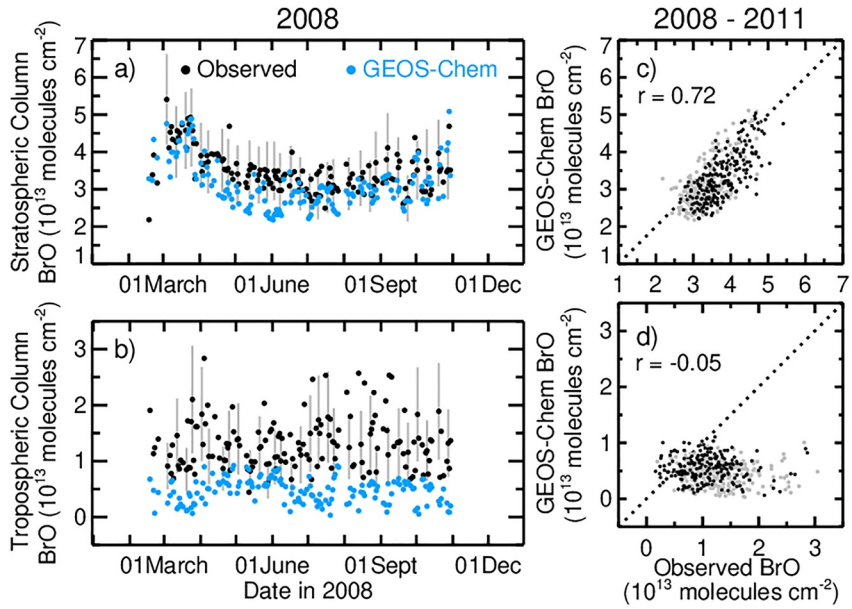

Figure 3. Modeled and measured stratospheric (a, c) and tropospheric (b, d) columns of BrO over Harestua, Norway for 2008 (a) and (b) and for 2008–2011 (c) and (d). (a) and (b) GEOS-Chem modeled columns are in blue, ground-based measurements are in black, and the uncertainty associated with the ground-based observations are included for every fifth measurement in gray. (c) and (d) In both panels, the 1 to 1 line is represented as a dotted line and the correlation coefficients between the two datasets are provided for boreal spring months (MAM). Points for the full year are shown in gray, while points associated with spring measurements are shown in black.

in Supporting Information S1). As described in Section 2.3, the twilight retrieval of the ground-based instrument allows for the separation of the column into tropospheric and stratospheric components, which is not available from nadir-viewing satellite instruments. Previous studies have reported close agreement between BrO^{OMI} and ground-based total (i.e., stratospheric + tropospheric) column BrO over Harestua, with a mean bias of $0.1 \pm 0.7 \times 10^{13}$ molecules cm^{-2} (Choi et al., 2018; Suleiman et al., 2019), indicating that the Harestua observations are a useful proxy for investigating the origin of the bias shown in Figure 2.

The seasonal trend in the stratospheric column of BrO observed by the ground-based instrument is captured by the simulation, as demonstrated for 2008 in Figure 3 (see Figure S1 in Supporting Information S1 for 2009–2011 time series). Overall, the model represents the stratospheric column of BrO over Harestua well with respect to ground-based observations although with a slight low bias (Figure 3a). For the spring months (i.e., March, April, and May, "MAM") 2008–2011, the correlation coefficient (r) between the stratospheric columns is 0.72 (Figure 3c), and the mean and standard deviation of the bias is $-0.4 \pm 0.4 \times 10^{13}$ molecules cm^{-2}. For February through October of the full time series, the mean and standard deviation of the bias in the stratospheric columns is $-0.3 \pm 0.5 \times 10^{13}$ molecules cm^{-2} ($r = 0.69$), representing a 10% low bias in the model with respect to observed stratospheric columns. The modeled tropospheric column of BrO is poorly correlated with the ground-based observations (Figure 3d) and has a mean bias of $-0.6 \pm 0.6 \times 10^{13}$ molecules cm^{-2} during spring months and $-0.7 \pm 0.6 \times 10^{13}$ molecules cm^{-2} overall. The total bias in BrO^{GC} is $-1.0 \pm 0.6 \times 10^{13}$ molecules cm^{-2} relative to the ground-based total column observations, consistent with the bias relative to BrO^{OMI} (Figure 2). Thus, low bias in BrO^{GC} has stratospheric and tropospheric origins over Harestua, with a larger contribution from the tropospheric column.

The tropospheric column of BrO shown in Figures 2b, 2d, and 3a is lower than reported by previous GEOS-Chem studies (Schmidt et al., 2016; Sherwen et al., 2016b). The tropospheric bromine source from open ocean sea salt aerosols is not included in our simulations, because previous studies report that sea salt debromination leads to overestimations in tropospheric BrO in comparison to observations over the northern hemisphere and in the tropical marine boundary layer (Schmidt et al., 2016). The addition of the HOBr + S(IV) reaction by Chen et al. (2017) contributes to the lower tropospheric columns reported by our study than previous publications, by increasing the wet deposition of Br_y species and thus reducing tropospheric Br_y by 50% relative to the

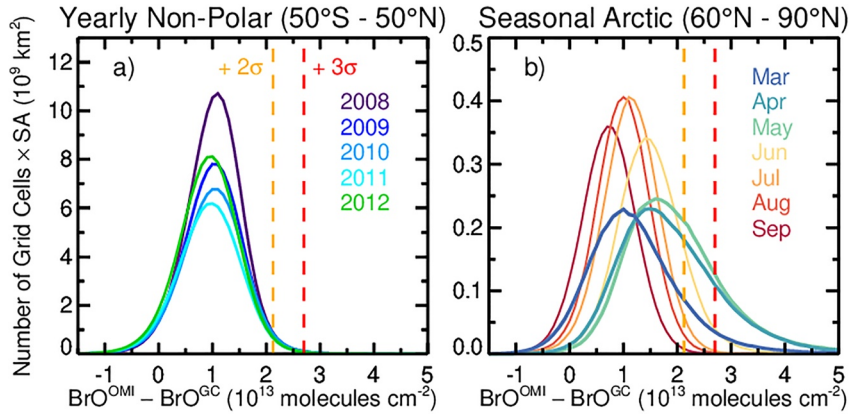

Figure 4. Histograms of the difference in column $BrO^{OMI} - BrO^{GC}$. Model grid cells are binned and counted for every 0.1×10^{13} molecules cm^{-2} and weighted by surface area (SA). Panel (a) shows the yearly distribution between latitudes of 50°S and 50°N, and panel (b) shows the monthly distribution for all years (2008–2012) between 50°N and 90°N. The dashed lines in both panels are the non-polar mean difference + 2σ (yellow) and + 3σ (red).

bromine mechanism presented by Schmidt et al. (2016). Revisions of the tropospheric halogen mechanism after version 12.0.1 have improved the representation of sea salt debromination through additional updates to the tropospheric sinks and heterogenous recycling of Br_y (X. Wang et al., 2021; Zhu et al., 2019). While open ocean sea salt aerosols are a significant source of Br_y in the marine boundary layer, this source is not sufficient to drive the low O_3 episodes observed during polar spring (Huang et al., 2020; Yang et al., 2020). Consequently, in the present study we do not attribute the entire difference between BrO^{OMI} and BrO^{GC} to polar processes, and we introduce a method for estimating polar emissions that is adaptable to later revisions in the GEOS-Chem mechanism.

We evaluate the distribution of BrO^{OMI} and BrO^{GC} differences outside of polar regions to minimize the impact of modeled biases in the stratosphere and tropospheric background on our interpretation of bromine explosion signals. Histograms of the difference between BrO^{OMI} and BrO^{GC} within non-polar (50°S and 50°N) and Arctic (50°N and 90°N) latitude bands are shown in Figure 4. The non-polar mean bias +3σ is 2.7×10^{13} molecules cm^{-2} (red dashed lines in Figure 4) and is initially used as a statistical bias threshold (σ_{BIAS}) to identify incidents of BrO^{TH}. This value is larger than 99.7% of the difference between OMI and GEOS-Chem columns of BrO observed in the tropics and midlatitudes. Since background values of tropospheric column BrO have been proposed that range from 0.5×10^{13} molecules cm^{-2} to 3×10^{13} molecules cm^{-2} (e.g., Hendrick et al., 2007; Schofield et al., 2004; Van Roozendael et al., 2002), if the majority of the $BrO^{OMI} - BrO^{GC}$ bias resides in the troposphere, the use of 2.7×10^{13} molecules cm^{-2} for σ_{BIAS} also effectively accounts for the upper-limit of background tropospheric columns reported by previous studies. Thus, the +3σ bias threshold primarily used in our study represents a lower limit for the occurrences of BrO^{TH}. In Section 3.3, a mean bias +2σ bias threshold (2.1×10^{13} molecules cm^{-2}, yellow dashed lines in Figure 4) is considered to assess the sensitivity of surface ozone and estimated polar emissions of Br_2 to the choice of a bias threshold. This lower threshold increases the detection of BrO^{TH} during March through June (Figure 4b) over the Arctic but is still larger than 98% of the bias observed over non-polar regions.

Our threshold method is similar to approaches taken by other studies that explored bromine explosion events using satellite retrievals and a stratospheric climatology of BrO (Bougoudis et al., 2020; Choi et al., 2018; Theys et al., 2011). The mode of the $BrO^{OMI} - BrO^{GC}$ distributions poleward of 50°N are within $\pm 1\sigma$ of the non-polar mean difference for each month (Figure 4b), indicating that analysis presented in Figure 4a is valid for the Arctic region. For spring months, there are more detections of BrO^{OMI} that exceed both the +3σ and +2σ thresholds than in other months, reflecting the detection of springtime bromine explosion events. However, there is a slight increase in the mode of the $BrO^{OMI} - BrO^{GC}$ differences during spring months, where in March the mode is centered around 1×10^{13} molecules cm^{-2}, and in April, May, and June the modes are near 1.6×10^{13} molecules cm^{-2}.

Columns of BrO retrieved by OMI and modeled by GEOS-Chem are shown for 3 days in April 2008 in Figure 5, characterizing the day-to-day variations of satellite and modeled BrO. For latitudes poleward of 50°N and for each day between 1 February and 30 June, regions where the difference between BrO^{OMI} and BrO^{GC} exceed σ_{BIAS}

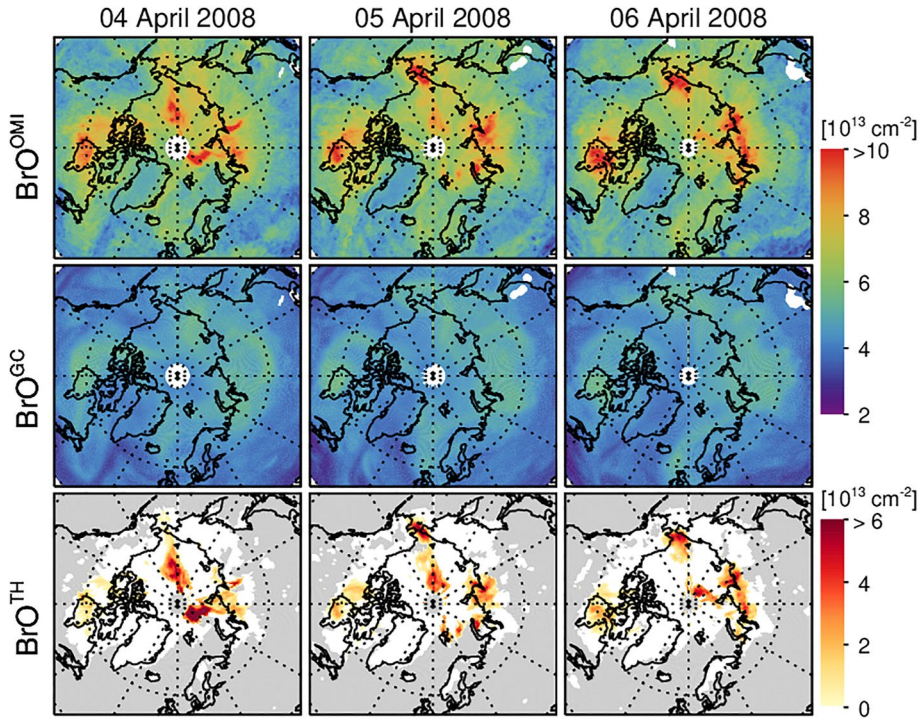

Figure 5. Columns of BrO over the northern hemisphere for 4–6 April 2008. The first row is retrieved BrO^{OMI}, the second row is modeled BrO^{GC} sampled at Ozone Monitoring Instrument (OMI) overpass time and averaged daily, and the third row is BrO^{TH} calculated according to Equation 7 ($+3\sigma$). The gray shading in the third row indicates where OMI data is filtered for the tropospheric retrievals.

($+3\sigma$) are identified as BrO^{TH}, as presented for the case study period of 4–6 April 2008 (third row of Figure 5). For reference, descriptions for the various abbreviations of BrO vertical columns, as defined in Sections 2.4 and 3.1, are provided in Table 1.

During conditions with elevated tropospheric BrO, the BrO^{OMI} retrieval underestimates the VCD due to the use of a mostly stratospheric a priori profile of BrO in the AMF calculation (Section 2.2). For each grid cell flagged as a tropospheric hotspot, AMF^{GC} is calculated using the overpass GEOS-Chem profile of BrO according to Section 2.2. The magnitude of BrO^{TH} is determined using the tropospheric residual method (e.g., Theys et al., 2011; Wagner & Platt, 1998):

$$BrO^{TH} = \frac{SCD^{OMI} - \left(BrO^{GC} + \sigma_{BIAS}\right) \times AMF^{GC}}{AMF^{TROP}} \quad (7)$$

with tropospheric air mass factors (AMF^{TROP}) prepared by Choi et al. (2012) using a BrO a priori profile based on aircraft measurements collected during the Arctic Research of the Composition of the Troposphere from Aircraft

Table 1
List of Abbreviations and Associated Descriptions for Vertical Columns of BrO

Abbreviation	Description
BrO^{OMI}	Total vertical column retrieved by the OMI satellite instrument
BrO^{GC}	Total vertical column simulated by GEOS with GEOS-Chem chemistry
BrO^{TH}	Tropospheric hotspot column, calculated according to Equation 7 from the difference between OMI retrieved and modeled BrO
BrO^{LT}	Lower tropospheric column, between the surface and ~2 km, from MAX-DOAS retrievals and smoothed modeled profiles, as described in Section 2.4
BrO^{200m}	Column between the surface and 200 m from MAX-DOAS retrievals and smoothed modeled profiles (Section 2.4)

and Satellite (ARCTAS) campaign. Two sets of daily fields of BrO^{TH} are produced with the value of σ_{BIAS} equal to 2.1×10^{13} molecules cm^{-2} ($+2\sigma$) and 2.7×10^{13} molecules cm^{-2} ($+3\sigma$). When calculating BrO^{TH}, OMI data is filtered using the additional criteria presented by Choi et al. (2018) described in Section 2.2. For all calculations of BrO^{TH}, values of BrO^{GC} and AMF^{GC} are determined by the base simulations with Br_y only supplied by photodecomposition of bromocarbons.

During boreal spring, spatial gradients in Arctic total column BrO^{GC} are driven by variations in the stratospheric column, as high values of column BrO are frequently associated with low tropopause heights, where stratospheric BrO compresses to lower altitudes (Begoin et al., 2010; Salawitch et al., 2010; Seo et al., 2020; Theys et al., 2011). Close correlation between simulated and ground-based observed stratospheric columns are found over Harestua (Figure 3c). As demonstrated in Figure 5, some enhancements in BrO^{OMI} with respect to the zonal mean are also reflected in broad features simulated in BrO^{GC}. For instance, portions of the hotspots in BrO^{OMI} over northern Canada are attributed to enhancements in the stratosphere rather than BrO^{TH}. Consequently, accurately accounting for variations in the stratospheric column, due to dynamics and chemical partitioning, is required to isolate regions of BrO^{TH}. Previous applications of the GEOS AGCM coupled to stratospheric chemistry modules have been found to produce realistic representations of stratospheric composition (e.g., Nielsen et al., 2017 and references therein). Description and evaluation of the GEOS-Chem stratospheric mechanism and chemical fields related to BrO are provided by Eastham et al. (2014) in an offline GEOS-Chem chemical transport model and by Knowland et al. (2022) in a similar online GEOS AGCM approach as the present study.

Here, we compare column simulations of O_3 and stratospheric NO_2 to OMI retrievals collected over the Arctic during boreal spring. The daytime stratospheric column of BrO has a positive correlation with total column O_3 due to similar responses in both columns to stratospheric dynamics (Salawitch et al., 2010; Theys et al., 2009). During boreal spring over the years 2008–2012, simulations of total column O_3 poleward of 50°N reproduce the magnitude and variability observed by OMI (Table S1 in Supporting Information S1). The mean and standard deviation of the relative bias between modeled and OMI column O_3 is $-2 \pm 3\%$, and r between the two columns is 0.97. The stratospheric partitioning of Br_y species into BrO is highly sensitive to mixing ratios of NO_2 via the termolecular reaction forming $BrONO_2$ (Sioris et al., 2006; Theys et al., 2009). In the northern hemisphere, stratospheric NO_2 increases from March to May, resulting in a decrease in daytime stratospheric BrO as more Br_y is partitioned into $BrONO_2$, as reflected in the stratospheric column of BrO over Harestua (Figure 3a and Figure S1 in Supporting Information S1). The GEOS-Chem mechanism captures the magnitude and seasonality of OMI stratospheric column NO_2 with a mean relative bias of $0.4 \pm 7\%$ and $r = 0.98$ (Table S1 in Supporting Information S1). However, uncertainties in modeling the stratospheric column of BrO remain that impact the interpretation of the tropospheric residual from satellite total column BrO (e.g., Wales et al., 2021), further motivating our use of a statistical threshold for interpreting the $BrO^{OMI} - BrO^{GC}$ residuals.

3.2. Calculating Arctic Flux of Br_2

For each year, BrO^{TH} is calculated according to Equation 7 for 1 February through 30 June and latitudes poleward of 50°N. While most bromine explosion events occur during spring months (Figure 4b), February and June are included to incorporate the beginning and end of the season. Daily flux of Br_2 (F_{Br2}) is calculated with a $1° \times 1°$ horizontal resolution based on the values of BrO^{TH}. The emitted Br_2 rapidly photolyzes during the day (reaction 5) and feeds into the Br and BrO (BrO_x) cycle (reactions 1 and 2). Throughout the day, the added Br_2 distributes among Br_y compounds, and Br_y is removed from the troposphere primarily via deposition of soluble species (Sherwen et al., 2016b).

To represent the observed values of BrO^{TH} in the model, we must account for how much of the emitted Br_2 will partition into Br_y species other than BrO and how long the added Br_y will remain in the system. As discussed in Section 3.1, there are continued updates implemented in more recent versions of the GEOS-Chem mechanism that impact the partitioning and lifetime of tropospheric Br_y (e.g., X. Wang et al., 2019b, 2021; Zhu et al., 2019). Additionally, similar emission schemes have been demonstrated to result in dissimilar Br_y fields and tropospheric columns of BrO depending on model configuration (Yang et al., 2020). Consequently, to evaluate the impact of satellite-detected BrO^{TH} fields on O_3 mixing ratios, we treat the estimated values of F_{Br2} as tuned to our current model setup and provide parameters to adjust the F_{Br2} fields for different model implementations.

We estimate the column of Br_y associated with each value of BrO^{TH} using the modeled ratio of tropospheric columns of $BrO:Br_y$ (χ_{Bry}). From the base GEOS-Chem simulation without Arctic emissions of Br_2 (Section 3.1),

χ_{Bry} at OMI overpass time has a linear relationship with SZA over latitudes poleward of 50°N, SZAs < 80°, and OMI reflectivity >0.6, as shown Figure S2a in Supporting Information S1. For each value of BrO^{TH}, χ_{Bry} is calculated as a linear function of the overpass SZA, where at a SZA of 40° the value of χ_{Bry} is about 0.3, and at a SZA of 70° the value of χ_{Bry} is closer to 0.5.

From preliminary tuning experiments conducted for the 2008 season, we found that: (a) modeled χ_{Bry} increases as BrO^{GC} increases with respect to the base simulation (ΔBrO^{GC}, Figure S2b in Supporting Information S1), and (b) a portion of the added Br_y remains in the system for longer than day, resulting in over representations of BrO^{TH} later in the season if the lifetime of Br_y is not considered. From Figure S2b in Supporting Information S1, for $\Delta BrO^{GC} > 4 \times 10^{13}$ molecules cm^{-2}, χ_{Bry} increases by 0.14 with respect to linearly calculated values (Figure S2a in Supporting Information S1). Thus, for the remainder of the study, χ_{Bry} is assumed to be 0.14 larger than estimated from the SZA linear fit for values of BrO^{TH} larger than 4×10^{13} molecules cm^{-2} (Figure S2b in Supporting Information S1):

$$\chi_{Br_y} = \begin{cases} 0.047 + SZA \times \frac{0.195}{30^\circ}, & BrO^{TH} < 4 \times 10^{13} \\ 0.187 + SZA \times \frac{0.195}{30^\circ}, & BrO^{TH} \geq 4 \times 10^{13} \end{cases} \quad (8)$$

To represent the impact of the tropospheric lifetime of Br_y on F_{Br2} calculations, the total mass of bromine associated with columns of BrO^{TH} is calculated over the Arctic (M_t) using χ_{Bry} for each day (t) in units of kg Br:

$$M_t = \sum \left(\frac{BrO^{TH}}{\chi_{Bry}} \times mass_{conv} \times SA_{grid} \right) \quad (9)$$

where SA_{grid} is the surface area of each 1° × 1° grid box, and $mass_{conv}$ converts molecules of BrO into kg Br. Since a portion of Br_y produced following the application of F_{Br2} remains in the system for longer than a day, only a fraction of M_t is due to new emissions. Based on preliminary simulations, approximately 50% of the Br_y produced following application of F_{Br2} at the surface is located between the surface and 500 m in altitude (Figure S1c in Supporting Information S1). The median springtime e-folding lifetime of Br_y integrated below 500 m (τ_{500m}) is used to approximate how long the added Br_y remains in the system, which was found to be 3 days over the relevant study area (i.e., latitudes >60°N) in the current model setup. The fraction of M_t that is due to fresh emissions (M_{frac}) is estimated daily according to:

$$M_{frac} = \frac{M_t - M_{t-1} \times e^{-\frac{1\,day}{\tau_{500m}}}}{M_t} \quad (10)$$

For each value of daily BrO^{TH}, F_{Br2} (kg m^{-2} s^{-1}) is calculated according to:

$$F_{Br_2} = \frac{BrO^{TH}}{\chi_{Bry}} \times \frac{mass_{conv}}{86,400\,s} \times M_{frac} \quad (11)$$

where BrO^{TH} is temporally and spatially resolved and M_{frac} is a daily value. Emissions are applied over 1 day (UTC) with no assumed diurnal variation.

However, the tropospheric lifetime of Br_y is not normally distributed and is highly variable in both time and space, with lifetimes generally increasing with increasing altitude. Since a single value is used for τ_{500m}, this method will not represent temporal and spatial gradients in the lifetime, and this assumption is a likely candidate for future development to improve the model representation of BrO^{TH} presented in Section 3.3. The application of F_{Br2} as a local source of BrO^{TH} without a diurnal profile is an additional simplification in our emission scheme that could impact the spatial distribution of the resulting modeled Br_y fields. Daytime photochemistry is required for release of Br_2 from snowpack surfaces (Custard et al., 2017; Pratt et al., 2013), and bromine explosion events are transported and sustained through heterogeneous recycling on aerosol and snowpack surfaces (Peterson et al., 2017; Zhao et al., 2016), propagating Br_y species from coastal sources to inland locations (Peterson et al., 2018; Simpson et al., 2005). While the emitted mass from Equation 11 is provided below with reference to previous studies, updates to the recycling efficiency would impact the mass of F_{Br2} needed to model BrO^{TH}, and near surface chemical conditions would alter χ_{Bry}, particularly during low O_3 conditions when the formation of BrO from reaction 1 decreases (S. Wang et al., 2019a; S. Wang & Pratt, 2017).

Table 2
Descriptions of Model Experiments With Different Sources of Br_y

Experiment	Time period	Description
Base	1 January 2008 to 31 December 2012	Continuous simulation with Br_y supplied by photodecomposition of organic bromine species and halons
ABr_3σ	1 February to 30 June 2008–2012	An additional Br_y source is provided with F_{Br2} fields calculated from values of BrO^{TH}, where $\sigma_{BIAS} = 2.7 \times 10^{13}$ molecules cm^{-2}
ABr_2σ	1 February to 30 June 2012	An additional Br_y source is provided with F_{Br2} fields calculated from values of BrO^{TH}, where $\sigma_{BIAS} = 2.1 \times 10^{13}$ molecules cm^{-2}

Between 2008 and 2012, the mean springtime emission of Br_2 determined from Equation 11 is 4.1 Gg Br $year^{-1}$, with values ranging between 3.0 and 6.1 Gg Br $year^{-1}$ with less than 0.2 Gg Br released during February and June combined. Over regions where BrO^{TH} is detected, the mean and standard deviation of F_{Br2} is $1.1 \pm 1 \times 10^8$ molecules cm^{-2} s^{-1} with values as high as 18×10^8 molecules cm^{-2} s^{-1}. Our OMI hotspot-based yearly emissions of Arctic Br_2 are significantly lower than the values reported by the Fernandez et al. (2019) bottom-up study, where the Br_y release from sea ice and heterogeneous recycling over the snowpack was estimated to be 270 Gg Br $year^{-1}$ over the Arctic, with 127 Gg Br emitted during boreal spring. However, our fluxes are similar in magnitude to the 0.7 and 12×10^8 molecules cm^{-2} s^{-1} range reported by Custard et al. (2017) based on measurements of Br_2 collected above an illuminated snowpack.

3.3. Simulations With Arctic Emissions of Br_2

Following the initial sensitivity simulation described in Section 3.2 to parameterize F_{Br2}, two experiments with an Arctic source of Br_y (hereafter referred to "ABr") are conducted with Br_2 emission fields defined by Equation 11. In the first experiment (ABr_3σ), BrO^{TH} is calculated using a value of 2.7×10^{13} molecules cm^{-2} (+3σ, Figure 4) for σ_{BIAS} in Equation 7, and in the second experiment (ABr_2σ), BrO^{TH} is determined using a value of 2.1×10^{13} molecules cm^{-2} (+2σ). ABr_3σ simulations were conducted each year (2008–2012) for 1 February to 30 June, while the ABr_2σ simulation is conducted for 1 year, 1 February to 30 June 2012. A summary of the model setups used in our study is provided in Table 2.

Due to SZA restrictions (Section 2.2), retrievals of OMI BrO are only available as far north as ~70°N on 1 March. While the detection of BrO^{TH} within February is consequently limited, each ABr simulation is initialized on 1 February with output from the Base simulation to allow a month to spin-up the system with emissions of F_{Br2}. Similarly, running the simulation through June verifies that the detection of BrO^{TH} ends in summer when snowmelt is expected to inhibit the propagation of bromine explosion events (Burd et al., 2017; Jeong et al., 2022). The ability of the ABr simulations to represent BrO^{TH} is assessed in Section 3.3.1, in Section 3.3.2 modeled BrO columns and surface O_3 levels are evaluated against measurements collected by instruments onboard O-Buoys, and simulations of surface O_3 over the Arctic are discussed in Section 3.3.3.

3.3.1. Modeling Hotspots of BrO

The differences in BrO^{GC} between the Base and ABr_3σ simulations (ΔBrO^{GC}) are shown in Figure 6 at OMI overpass time for the same 3 days illustrated in Figure 5. Comparisons between BrO columns for 1 March to 31 May 2008 are provided in Supporting Information S1, Movie S1. The local spatial features of BrO^{TH} are generally reproduced by ΔBrO^{GC}, as seen in Figure 5. While simulations of ΔBrO^{GC} are initially low with respect to BrO^{TH} along the Russian coast on 6 April 2008, high values of BrO^{TH} are simulated in this area on the following days (Movie S1). Also, during 4–6 April 2008, the large values of ΔBrO^{GC} over Hudson Bay in northern Canada overestimate the local BrO^{TH} features. During this time period, there are high values of BrO^{OMI} with similar spatial patterns to the ΔBrO^{GC} amplification. However, due to larger values of BrO^{GC}, relatively small amounts of BrO^{OMI} are attributed to BrO^{TH} over this region (Figure 5). Finally, upon application of F_{Br2} in GEOS-Chem, isolated but large decreases in surface layer O_3 are modeled, with values on 4 April 2008 reaching up to 21 ppb over northern Canada, a 55% decrease relative to the Base simulation (last row in Figure 6). As discussed further

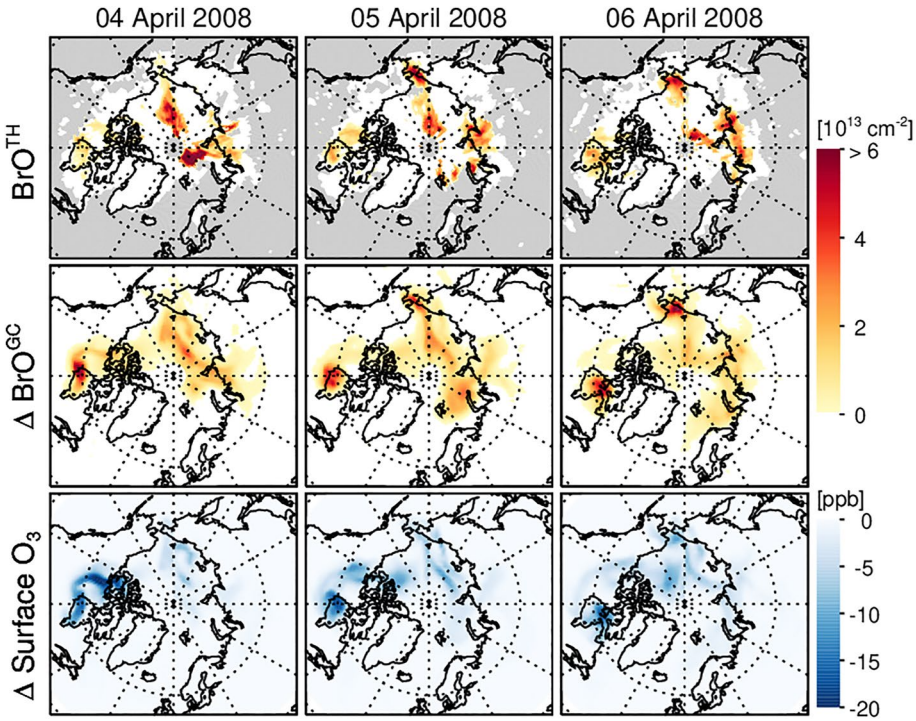

Figure 6. Column BrO and surface O_3 over the northern hemisphere for 4–6 April 2008. The first row is BrO^{TH} as shown in Figure 5, the second row is ΔBrO^{GC} sampled at Ozone Monitoring Instrument overpass time and averaged per day if multiple overpasses are present, and the third row is the decrease in surface layer O_3 for ABr_3σ simulations.

in Section 3.3.3, the background mixing ratios of O_3 are simulated by both Base and ABr_3σ experiments, but there is an observed 50% decrease in surface O_3 over Utqiaġvik, Alaska on 7 April 2008 that is not represented in the ABr_3σ emission scheme.

As discussed with the examples given in Figure 6, the parameterized emissions are able to capture some of the features detected by OMI, but the timing and exact location of the features are sometimes displaced from BrO^{TH}. To assess the daily performance of the ΔBrO^{GC} simulations with respect to BrO^{TH}, we determine the normalized mean bias (NMB):

$$\mathrm{NMB} = \frac{\sum\left(\Delta BrO^{GC} - BrO^{TH}\right)}{\sum BrO^{TH}} \tag{12}$$

for 1 March to 31 May over the years simulated with the ABr_3σ emission scheme (2008–2012). Overall, values of ΔBrO^{GC} are typically lower than BrO^{TH} with a NMB of −5% and $r = 0.55$, as shown in Table 3. Performance varies across the different years, and the daily, spatially resolved correlation coefficients are generally comparable to the results reported by Bougoudis et al. (2022), who trained an artificial neural network using satellite retrieved tropospheric columns of BrO. However, if NMB is assessed per month, ΔBrO^{GC} is consistently low with respect to

Table 3
The Normalized Mean Bias and r Between Daily, Spatially Resolved Values of BrO^{TH} and ΔBrO^{GC} Sampled at Ozone Monitoring Instrument Overpass Times

	ABr_3σ NMB % (r)						ABr_2σ NMB % (r)
	2008–2012	2008	2009	2010	2011	2012	2012
March	−49 (0.48)	−25 (0.45)	−49 (0.57)	−59 (0.54)	−58 (0.54)	−63 (0.50)	−52 (0.55)
April	8 (0.46)	−8 (0.50)	32 (0.44)	22 (0.37)	3 (0.44)	−8 (0.60)	−1 (0.68)
May	−8 (0.67)	−12 (0.65)	−8 (0.64)	−18 (0.61)	7 (0.68)	−16 (0.67)	−16 (0.71)
MAM	−5 (0.55)	−12 (0.53)	5 (0.58)	−9 (0.44)	1 (0.57)	−19 (0.58)	−14 (0.66)

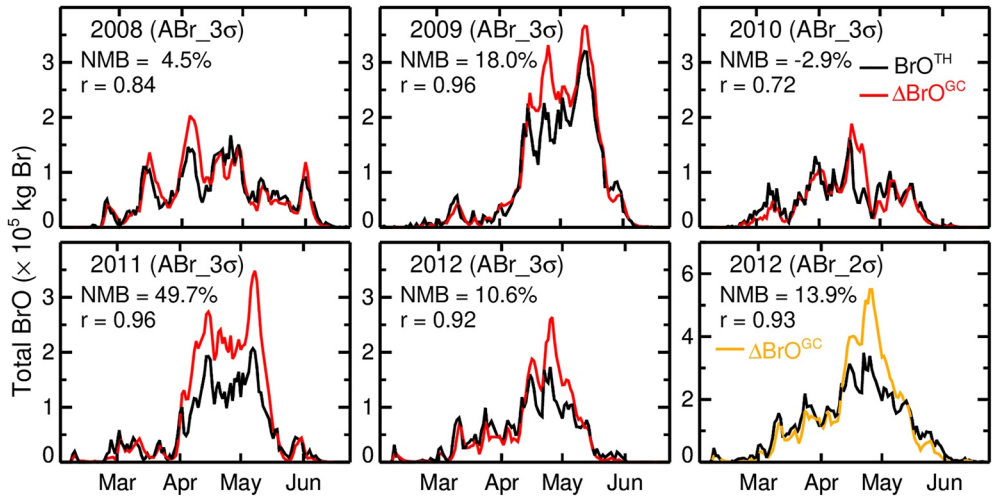

Figure 7. Daily mass of BrO^{TH} (black) and ΔBrO^{GC} in red from ABr_3σ simulations for 1 February to 30 June, 2008–2012 and in yellow from the ABr_2σ simulation for 2012. Values for the normalized mean bias and correlation coefficients are provided each year for spring months (i.e., 1 March to 31 May).

BrO^{TH} during March (NMB = –49%) with better performance achieved in April and May (NMB = ±8%), indicating that aspects of our F_{Br2} emission scheme struggle to reproduce detected BrO^{TH} in early spring.

Values of F_{Br2} were parameterized based on the mass of BrO detected by BrO^{TH} and the assumed mass of Br_y (in units of kg Br) associated with these BrO columns (Equation 9). We further assess the ability of our ABr_3σ emission scheme to reproduce the OMI-based BrO^{TH} signals by comparing the total, daily mass of bromine contained in BrO^{TH} and ΔBrO^{GC} shown as black and red lines, respectively, in Figure 7 for 2008–2012. Since the mass shown in Figure 7 is only for that contained in BrO (i.e., χ_{Bry} is not considered), the total mass of Br_y associated with the hotspots is larger than shown. Additionally, as demonstrated in Figure 2, there are portions of the Arctic not visible to the OMI satellite during early spring where daytime SZAs are too large for the retrieval of BrO. Consequently, as discussed in more detail in Section 3.3.3, our detection of bromine explosion events will be limited to lower latitudes during this time.

The simulated total mass of ΔBrO^{GC} captures the daily magnitude and variability of BrO^{TH} with a NMB of 15% and $r = 0.92$ over 1 March through 31 May for all 5 years. As seen with the spatially resolved features, skill at simulating springtime daily mass of BrO^{TH} varies from year-to-year, with NMB values ranging from −3% up to +50% and $0.72 \leq r \leq 0.96$. Periods where ΔBrO^{GC} overrepresents BrO^{TH} are typically accompanied by increases in the mass of Br_y larger than the mass of M_t calculated by Equation 9, suggesting that our treatment of the lifetime of Br_y in Equation 10 contributes to the high values of ΔBrO^{GC}.

To determine the sensitivity of our simulations to the magnitude of σ_{BIAS} used to calculate BrO^{TH} (Equation 7), an experiment is conducted using a threshold that is the non-polar mean bias +2σ (yellow dashed line in Figure 4, Table 2). This is a 0.6×10^{13} molecules cm^{-2} reduction in σ_{BIAS} with respect to the +3σ threshold used in the ABr_3σ simulation. Values of BrO^{TH} and F_{Br2} (Equation 11) are recalculated with the lower threshold and implemented for 1 February through 30 June 2012 only ("ABr_2σ," Table 2). The yearly emissions for the ABr_2σ scenario are 9.5 Gg Br $year^{-1}$, double the emissions calculated for the ABr_3σ simulation in 2012 (4.3 Gg Br $year^{-1}$). The daily mass of bromine contained in BrO^{TH} and ΔBrO^{GC} are in good agreement with NMB = 8% and $r = 0.93$, shown in yellow in Figure 7. These values are similar to the ABr_3σ 2012 results (NMB = 11% and $r = 0.92$), indicating that the method introduced in Section 3.2 performs consistently with larger quantities of BrO^{TH}. However, as shown in Table 3, there is still a negative bias with respect to the spatially resolved columns, indicating that restricting our F_{Br2} calculations to the total mass detected in BrO^{TH} results in an overall low bias with respect to the individual features.

3.3.2. O-Buoy Measurements of BrO and O_3

Our detection of elevated BrO is assessed by comparing OMI-based columns of BrO^{TH} to retrievals of BrO columns in the lower troposphere, BrO^{LT}, collected by MAX-DOAS instruments onboard ice-tethered O-Buoys. As discussed in Section 2.4, the MAX-DOAS retrievals of BrO^{LT} and BrO^{200m} are respectively most sensitive to the lowest 2 km and 200 m above the surface (Table 1). Since the ABr_2σ simulation was conducted only for

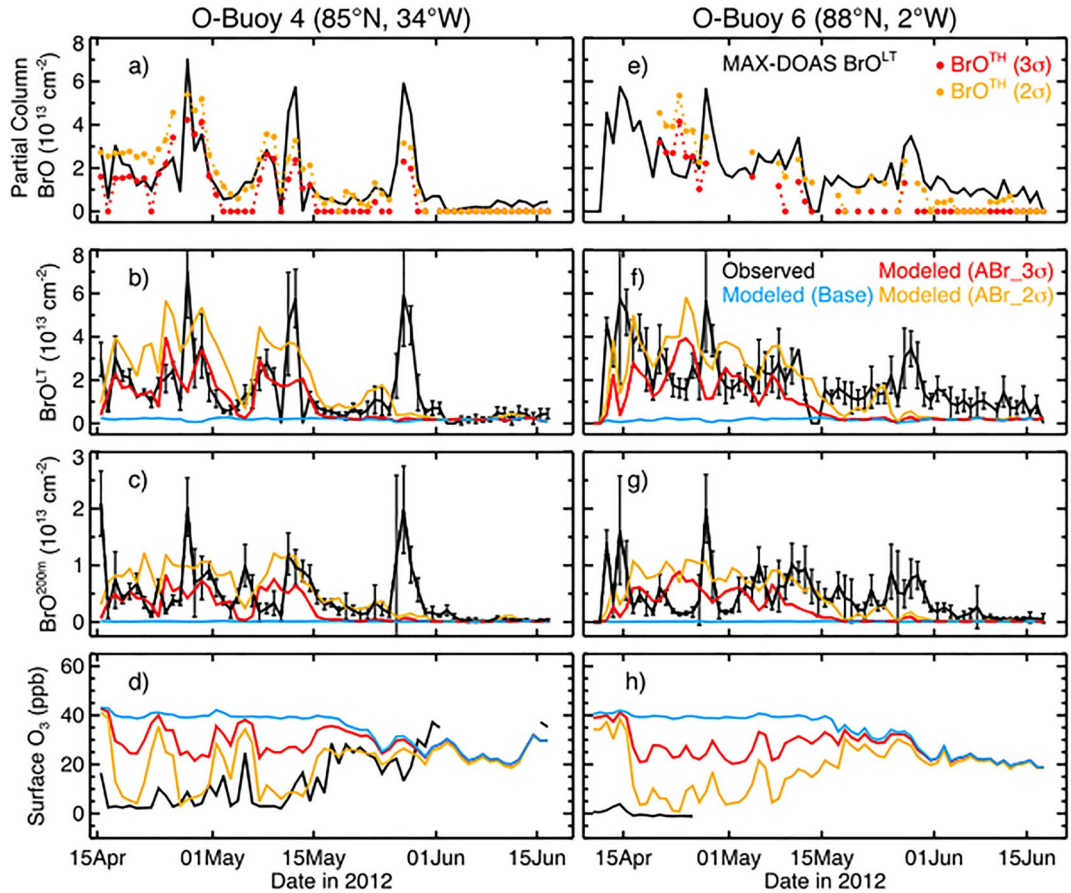

Figure 8. Daily mean observations and modeled parameters sampled along the 2012 (a–d) O-Buoy 4 and (e–g) O-Buoy 6 tracks. In panels (a) and (e), points are OMI-based values of BrO^{TH} along the buoy tracks and black lines are multi-axis differential optical absorption spectroscopy (MAX-DOAS) BrO^{LT}. In the remaining panels, black lines are buoy-based observations, and the blue, red, and yellow lines are respectively the simulations for the Base, ABr_3σ, and ABr_2σ scenarios. BrO^{LT} is shown in panels (b) and (f), where the MAX-DOAS observed values are repeated from panels (a and e). BrO^{200m} is shown in panels (c and g), and surface O_3 is in panels (d) and (h). All BrO partial columns are daytime (SZA < 80°), daily means, error bars represent the standard deviation about the MAX-DOAS daily mean, and modeled partial columns are smoothed using MAX-DOAS averaging kernels.

2012 (Table 2), O-Buoy tracks for this year are highlighted in Figure 8 and Table 4, with 2011 tracks Figure S3 in Supporting Information S1 and Table S2 in Supporting Information S1.

Daily mean BrO^{TH} for both thresholds of σ_{BIAS} are shown along the 2012 O-Buoy tracks in Figures 8a and 8e, where missing points of BrO^{TH} are due to filtering of the OMI data, as described in Section 2.2. Estimations of BrO^{TH} are well correlated with daytime, daily means of MAX-DOAS BrO^{LT} with $r = 0.73$ during 2012 for both values of σ_{BIAS}. Similarly, the correlation for the full 2011–2012 time period is $r = 0.66$ (Table S2 in Supporting Information S1). Correlation with MAX-DOAS BrO^{LT} weakens over the O-Buoy 3 track during 2011, located in Hudson Bay (Figure 1), where all values of BrO^{TH} underestimate the observed BrO^{LT} columns or do not detect elevated columns with respect to the $BrO^{OMI} - BrO^{GC}$ mean bias (Figure S3e in Supporting Information S1). However, the overall good correlation ($r = 0.66$, Table S2 in Supporting Information S1) between BrO^{TH} and the observed BrO^{LT} indicates that despite the persistent background bias between BrO^{OMI} and BrO^{GC}, our method for calculating BrO^{TH} is able to isolate BrO signals associated with the lower troposphere. While lowering the value of σ_{BIAS} does not significantly impact the correlation between BrO^{TH} and the buoy-based BrO^{LT} retrievals, the lower threshold reduces the number of false-negative detections along all four tracks.

Even though retrievals of BrO^{LT} may represent BrO features that have a broad enough horizontal structure to be detected by satellite instruments, ODEs are responsive to near surface BrO. Previous studies have found instances where elevations in near surface BrO are not vertically mixed and have sharp horizontal gradients that are not detectable by satellite retrievals (e.g., Peterson et al., 2015; Simpson et al., 2017). The correlation between BrO^{TH}

Table 4
Statistics Between Daytime Mean BrO Columns Retrieved From the Multi-Axis Differential Optical Absorption Spectroscopy (MAX-DOAS) Instrument and the Partial Columns Produced by the Present Study (Ozone Monitoring Instrument [OMI] and Model-Based) That Have Been Sampled Along O-Buoy Deployments in 2012

	Study partial column				
MAX-DOAS column	Variable	Source	Mean bias (10^{13} molecules cm^{-2})	NMB (%)	r
BrO^{LT}	BrO^{TH}	OMI-based (+3σ)	–0.8 ± 1	−50	0.73
BrO^{LT}	BrO^{LT}	ABr_3σ modeled	–0.8 ± 1	−46	0.37
BrO^{200m}	BrO^{200m}	ABr_3σ modeled	–0.2 ± 0.5	−50	0.16
BrO^{LT}	BrO^{TH}	OMI-based (+2σ)	–0.08 ± 1	−5	0.73
BrO^{LT}	BrO^{LT}	ABr_2σ modeled	0.04 ± 2	+2	0.45
BrO^{200m}	BrO^{200m}	ABr_2σ modeled	0.006 ± 0.5	+1	0.28

calculations and MAX-DOAS BrO^{200m} columns is 0.54 and 0.60 respectively for the +3σ and 2σ values (Table S2 in Supporting Information S1), demonstrating a reduction in the correlation between the satellite-based detection of elevated BrO and near-surface observations.

Modeled profiles of BrO are scaled according to the retrieval sensitivity (Swanson et al., 2022) to calculate modeled columns of BrO^{LT} (Figures 8b and 8f) and BrO^{200m} (Figures 8c and 8g). Simulated columns of BrO^{LT} are less correlated with MAX-DOAS retrievals than observed for the BrO^{TH} analysis, with r values of 0.37 and 0.45 for the ABr_3σ and ABr_2σ scenarios, respectively, and correlation between observed and modeled BrO^{200m} columns is poor (Table 4). As demonstrated with Figure 7, these simulations perform well with respect to BrO^{TH} when assessed over the whole study region but as shown in Figure 6 and Table 3, do not always capture the timing and magnitude of local features, particularly during March.

Overall, the magnitude of BrO columns from the ABr_2σ simulation is in closer agreement with the MAX-DOAS observations than the ABr_3σ simulation (Table 4). The mean bias between the simulated and MAX-DOAS BrO^{LT} columns is $0.04 \pm 2 \times 10^{13}$ molecules cm^{-2} (NMB = 2%) for the ABr_2σ scenario and $-0.8 \pm 1 \times 10^{13}$ molecules cm^{-2} (NMB = –50%) for the ABr_3σ scenario (Table 4). This demonstrates that the ABr_2σ simulation generally represent the magnitude of BrO along these buoy tracks, albeit with a slight overestimate of BrO between 15 April and 15 May 2012 and an underrepresentation of detected peaks in BrO later in the season (Figure 8). While the correlation of the simulations is poor with respect the MAX-DOAS retrievals, the NMB values are generally consistent across each σ_{BIAS} scenario.

Along each 2012 buoy track, there are periods where surface layer O_3 mixing ratios in the ABr_3σ simulations (shown in red in Figures 8d and 8h) decrease by over 10 ppb (about 25%) with respect to the Base simulation (shown in blue). These decreases in surface O_3 do not exceed 20 ppb (i.e., 50%), and the near-zero mixing ratios measured during the O-Buoy tracks are not reproduced by the ABr_3σ simulation (Figures 8d and 8h and Figure S3d in Supporting Information S1 for O-Buoy 2). For the ABr_2σ scenario (shown in yellow), periods of O_3 mixing ratios <10 ppb are simulated over both O-Buoy 4 and 6, and measurements are well represented over the O-Buoy 4 for only the ABr_2σ experiment, demonstrating the sensitivity of ozone simulations to the choice of σ_{BIAS} in interpreting BrO^{TH}. However, periods in April 2012 where observed ozone depletion episodes are portrayed are associated with times when local BrO^{200m} is overestimated by the ABr_2σ simulation (Figure 8c).

3.3.3. Evaluation of Surface Ozone Simulations

To further investigate the impact of the Arctic Br_2 emissions, we sample model output at the locations of three coastal stations that monitor surface O_3 (Section 2.5, Figure 1). The daily mean observations for February through June 2012 from these stations are shown in black in Figure 9, and simulations of surface-layer O_3 sampled at the closest grid-box to these three locations are shown for the Base (blue), ABr_3σ (red), and ABr_2σ (yellow) simulations (Table 2). Similar panels are shown for 2008–2011 in Figure S4 in Supporting Information S1. The gray shading in Figure 9 indicates when retrievals of BrO^{OMI} are not available over each station due to daytime SZAs > 80°. Over regions where OMI retrievals of BrO are unavailable, either due to filtering criteria or missing overpasses, values of BrO^{TH} are treated as zero for the day. Because of the 80° SZA limit, OMI observations are available only as far north as 72°N on 1 March and 85°N on 1 April 2012.

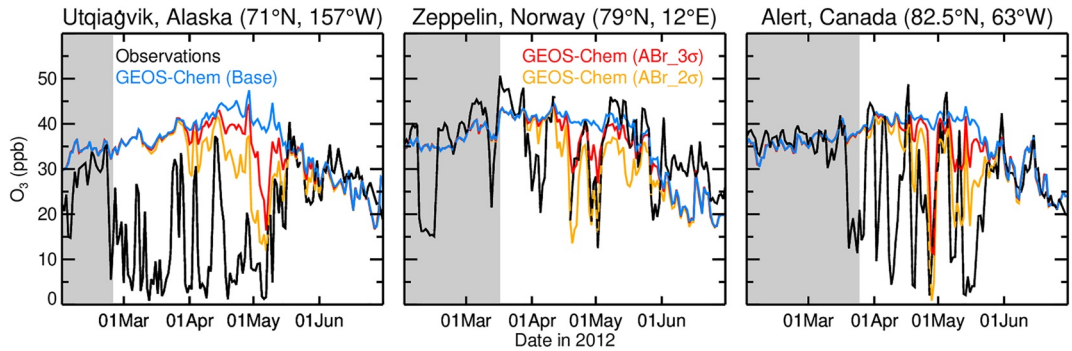

Figure 9. Daily mean modeled and observed surface O_3 over three stations during spring 2012. Ozone observations are shown in black, the Base GEOS-Chem simulation is shown in blue, ABr_3σ simulation is in red, and the ABr_2σ threshold sensitivity scenario in yellow. The gray shading in each panel indicates time periods where SZAs > 80° at local noon. The locations of these stations are shown in Figure 1.

Generally, all simulations accurately represent background mixing ratios of O_3 during February and June, with the exception of a low model bias over the Zeppelin station during June (Figure 9). In April and May 2012, the application of F_{Br2} results in lower values of surface O_3 simulated over all three stations, and an ozone depletion episode is simulated over Alert in late April with both σ_{BIAS}. For 2008 through 2012 the impact of the ABr_3σ emissions on surface O_3 over the coastal stations is generally small (red lines in Figure 9 and Figure S4 in Supporting Information S1). Consistent with results over O-Buoy tracks in the Arctic Ocean (Figure 8), more ozone loss is found in the ABr_2σ (yellow lines) than in the ABr_3σ simulation. However, decreasing σ_{BIAS} for the detection of BrO^{TH} has only a minor impact on surface layer O_3 over coastal stations during March 2012, and despite lower SZAs at Utqiaġvik in late winter compared to Zeppelin and Alert, the low ozone events over Utqiaġvik are still not represented in the ABr_2σ scenario (Figure 9).

Utqiaġvik, Alaska has been the location of numerous studies investigating bromine explosion events, including two field campaigns during the springs of 2009 and 2012. Previous studies have found that satellite instruments may underestimate elevations in near-surface BrO under meteorological conditions associated with a stable boundary layer (Peterson et al., 2015; Sihler et al., 2012; Swanson et al., 2020). During March 2009, few cases of elevated BrO are detected over Utqiaġvik by our OMI-based values of BrO^{TH}, as shown in Figure S5a in Supporting Information S1. The Ocean-Atmosphere-Sea Ice-Snowpack (OASIS) campaign, conducted in spring 2009, observed enhancements in near-surface mixing ratios of BrO, HOBr, and Br_2 over Utqiaġvik using an in-situ chemical ionization mass spectrometry (CIMS) instrument, with mixing ratios of BrO as high as 40 ppt detected by CIMS and long pass DOAS (LP-DOAS) instruments (Liao et al., 2011, 2012). Additionally, periods of sustained, low boundary layer heights were reported between March 14 and April 7 of the OASIS campaign (Boylan et al., 2014), impacting the ability to detect near-surface enhancements of brominated species using OMI retrievals. During the 2012 Bromine, Ozone, and Mercury Experiment (BROMEX) campaign (Pratt et al., 2013; S. Wang et al., 2019a), shallow BrO events were also frequently detected (Peterson et al., 2015; Simpson et al., 2017); however, during this campaign values of BrO^{TH} were identified over Utqiaġvik but were consistently underrepresented by the ABr simulations (Figure S5b in Supporting Information S1), consistent with findings presented in Section 3.3.1 (Table 3). In addition to the modeling limitations listed in Section 3.2, multiple studies utilizing OASIS and BROMEX data have reinforced the idea that recycling on snowpack surfaces is necessary to increase the catalytic efficiency of bromine-mediated ozone loss and model observations of O_3 and Br_y species collected over Utqiaġvik (Ahmed et al., 2022; Frieß et al., 2011; Marelle et al., 2021; Thompson et al., 2017; X. Wang et al., 2019b).

To evaluate the impact of F_{Br2} over the whole study region, monthly mean column BrO and surface-layer O_3 statistics are shown in Figure 10 for the 2012 ABr_3σ simulation. For reference, these panels were chosen to be comparable to previous GEOS-Chem studies that implemented an Arctic blowing snow source of bromine (Huang et al., 2020). Similar figures are shown in Supporting Information S1 for the earlier years (Figures S6–S9 in Supporting Information S1), and in Figure 11 for the 2012 ABr_2σ simulation. From the analysis presented in Figure 7, the total mass of daily ΔBrO^{GC} over the study region is well correlated with, but with a slight high bias with respect to, detected BrO^{TH} ($r = 0.92$; NMB = 11%). This high bias is seen near the North Pole in April

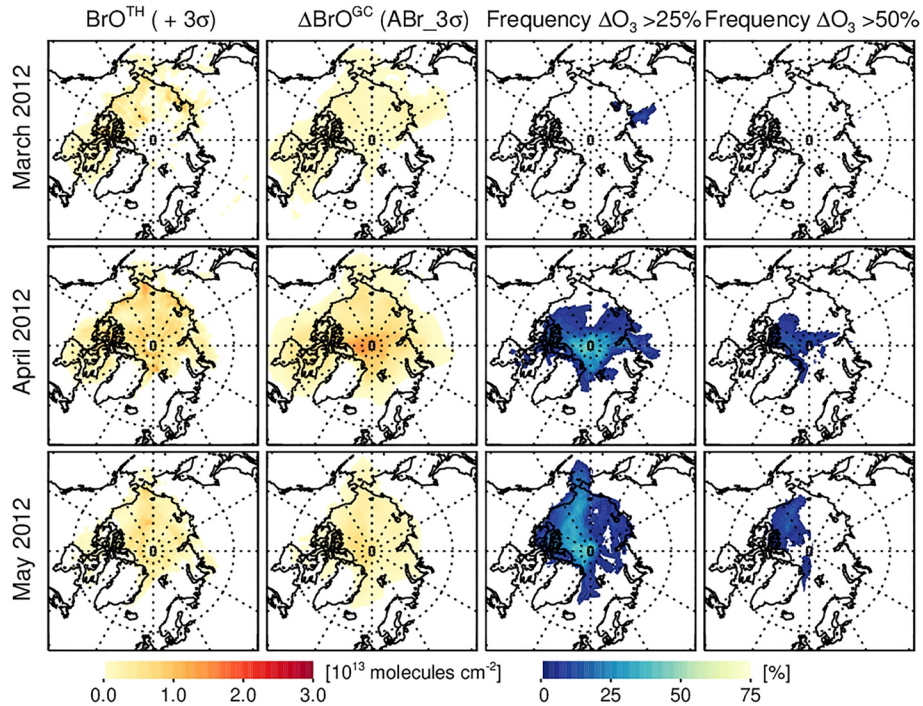

Figure 10. Monthly column BrO and surface layer O_3 statistics for 2012. The first and second columns respectively are monthly mean BrO^{TH} and ΔBrO^{GC} for the ABr_3σ scenario. The third and fourth columns show how frequently there are large (>25 and 50%, respectively) decreases in modeled surface layer ozone between Base and ABr_3σ simulations.

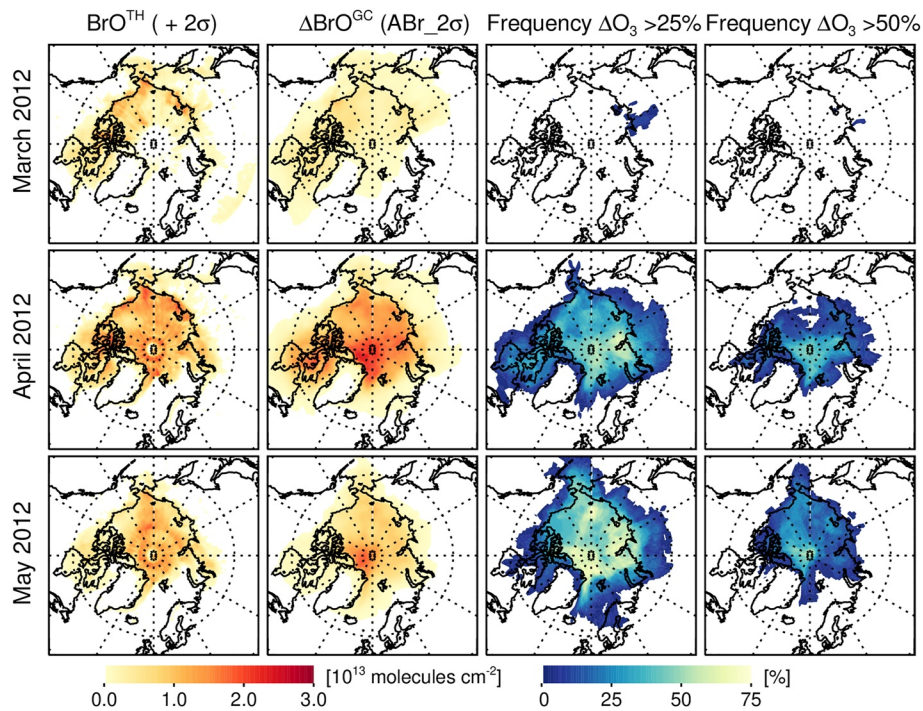

Figure 11. Same as Figure 10 but for the ABr_2σ threshold sensitivity simulation.

monthly mean ΔBrO^{GC} in both Figures 10 and 11. Also, the ΔBrO^{GC} fields have lost some of the detail present in the BrO^{TH} monthly mean map, particularly along the northern Alaskan and Siberian coastlines in Figure 11, reflecting the low bias in ΔBrO^{GC} with respect to spatially resolved BrO^{TH} and contributing to the high bias in surface ozone over Utqiaġvik (Table 3, Figure 9).

For latitudes poleward of 60°N, the monthly mean decreases in ABr_3σ surface ozone (ΔO_3) relative to the Base simulation are 0.6%, 7.2%, and 8.5% for March, April, and May 2012, respectively. For the ABr_2σ sensitivity scenario, these values are 1.4%, 18.5%, and 21.6%. As demonstrated in Figure 6, the application of a lower-limit estimate to the polar flux of Br_2 results in isolated but large values of ΔO_3 that are not captured by monthly mean calculations. In Figures 10 and 11, we highlight how frequently there are large decreases in surface O_3, defined as where ΔO_3 is greater than 25% or 50%.

Overall, larger amounts of O_3 loss are simulated later in the season than in early spring, as seen over coastal stations (Figure 9). During March 2012, there are no events simulated where $\Delta O_3 > 50\%$ and infrequent events with $\Delta O_3 > 25\%$ for both scenarios. Monthly statistics for the 2008–2011 time periods (Figures S6–S9 in Supporting Information S1), similarly demonstrate that periods of large O_3 loss are infrequently modeled during March ABr_3σ simulations. Additionally, there is interannual variability in the frequency of these events in late spring that reflects the variability in detected BrO^{TH} (Figure 7), with more frequent events detected in 2009 and 2011 than in 2008 and 2010. While in ABr_3σ simulations, events where $\Delta O_3 > 50\%$ are relatively infrequent during April and May 2012, there are occurrences of $\Delta O_3 > 25\%$ over most of the Arctic Ocean during this period, with locations near the pole experiencing $\Delta O_3 > 25\%$ for roughly half of both months (Figure 10). During April and May 2012, occurrences of large ΔO_3 from the ABr_2σ scenario cover a greater SA and last for more days (Figure 11) than in ABr_3σ, with more frequent decreases in surface O_3 simulated over the Arctic Ocean than inland.

Studies that evaluated process-based emissions of bromine explosion events using satellite retrieved BrO columns have frequently focused on case studies of BrO plumes or the monthly mean seasonality of the tropospheric columns (e.g., Fernandez et al., 2019; Herrmann et al., 2021; X. Zhao et al., 2016). The study by Huang et al. (2020) implemented a blowing snow source of Br_y within the GEOS-Chem chemical transport model and was able to reproduce monthly mean OMI tropospheric columns of BrO with NMB = 2% and $r = 0.76$. This study produced larger mean reductions in surface O_3 than simulated by our study but report frequently missing and underrepresenting ODEs. In our interpretation of the satellite columns, a bias threshold is removed from the $BrO^{OMI} - BrO^{GC}$ residual, rather than using the full tropospheric column. This approach was chosen to reduce misattribution of aloft BrO to near surface events. Previous studies have reported similar challenges in capturing the magnitude of the BrO vertical column due to uncertainties in the stratospheric and free tropospheric columns (Falk & Sinnhuber, 2018; Fernandez et al., 2019; Toyota et al., 2011). While part of the difficulty in modeling surface ozone reductions in our study is due to negative biases between co-located simulated ΔBrO^{GC} and BrO^{TH} (Table 3), less BrO^{TH} mass is detected in March than later in the season (Figure 7), when a portion of near-surface BrO is not expected to be detected by satellite retrievals, and OMI has limited coverage of the Arctic due to SZA restrictions. Lastly, even though reducing the magnitude of σ_{BIAS} does resolve the biases in O_3 with respect to coastal measurements in 2012 (Figure 9), it does impact how frequently 50% decreases in surface O_3 are simulated over the Arctic Ocean (Figure 11).

4. Conclusions

We introduce a novel method for estimating emissions of Br_2 associated with bromine explosion events using OMI retrievals of column BrO (BrO^{OMI}) and the GEOS-Chem (v12.0.1) chemical mechanism. Profiles of BrO are simulated for 1 January 2008 to 31 December 2012 using the GEOS AGCM, coupled to the GEOS-Chem chemical module and replayed to the MERRA-2 meteorological reanalysis. These simulations are conducted with the full stratospheric and tropospheric GEOS-Chem mechanism with an updated stratospheric mechanism that was recently evaluated in a similar GEOS setup (Knowland et al., 2022). Emissions of Br_2 are estimated for each day at the location of OMI-based tropospheric hotspots of BrO (BrO^{TH}) using parameters calculated within the chemical mechanism to account for the partitioning of total Br_y into observable BrO and the atmospheric lifetime of Br_y in the lower troposphere. Since updates to the GEOS-Chem tropospheric mechanism since version 12.0.1 are expected to impact the Br_y partitioning and resulting lifetime within the model (e.g., X. Wang et al., 2021; Zhu et al., 2019), these two parameters may be adjusted to adapt this emission scheme in future modeling efforts.

Modeled columns of BrO (BrO^{GC}) in Base simulations without an Arctic source of Br_y are systematically lower than satellite retrieved BrO^{OMI}. The mean and standard deviation (σ) of the difference in the two

columns ($BrO^{OMI} - BrO^{GC}$) outside of regions impacted by polar bromine explosion events (i.e., 50°S–50°N) is $1.0 \pm 0.6 \times 10^{13}$ molecules cm^{-2}, which is in part due to the sea salt aerosol source of tropospheric Br_y being turned off in our implementation of the GEOS-Chem mechanism. The stratospheric portion of BrO^{GC} is well correlated ($r = 0.72$) with ground-based retrievals of BrO over Harestua, Norway (61°N) during boreal spring with a mean bias of $-0.4 \pm 0.4 \times 10^{13}$ molecules cm^{-2}. Meanwhile, the tropospheric portion of BrO^{GC} is not correlated with the ground-based measurements ($r = -0.05$) with a mean bias of $-0.6 \pm 0.6 \times 10^{13}$ molecules cm^{-2}. This indicates that while most of the bias in BrO^{GC} over Harestua originates from the troposphere, consistent with the lack of a sea salt aerosol debromination source in our simulations, there is potentially a non-negligible stratospheric contribution from the bias in the total columns.

A statistical threshold is used to isolate columns of BrO^{TH} from OMI retrievals over the Arctic that are likely associated with springtime bromine explosion events. To account for modeled uncertainties in the stratospheric and background tropospheric column of BrO, the preliminary threshold was chosen to be the non-polar $BrO^{OMI} - BrO^{GC}$ mean bias $+3\sigma$ (2.7×10^{13} molecules cm^{-2}). The resulting values of BrO^{TH} represent a lower limit for the impact of polar emissions on BrO^{OMI} signals. A sensitivity study is conducted by reducing the bias threshold to the non-polar mean bias $+2\sigma$ (2.1×10^{13} molecules cm^{-2}). The parameterized Arctic emissions of Br_2 are calculated from BrO^{TH} and applied in the model for February through June over 2008–2012 using the 3σ threshold (ABr_3σ) and over 2012 using the 2σ threshold (ABr_2σ). Overall, the increase in BrO^{GC} in Arctic bromine with respect to Base simulations (ΔBrO^{GC}) captures the magnitude and daily variability of BrO^{TH} with a NMB of −5% ($r = 0.55$). The skill at capturing BrO^{TH} is maintained for the 2012 ABr_2σ simulation, but in all simulations values of BrO^{TH} are significantly underrepresented during March (NMB = −49%).

During 2011 and 2012, both values of BrO^{TH} (3σ and 2σ-based) are correlated with lower tropospheric columns of BrO (BrO^{LT}) collected by MAX-DOAS instruments onboard ice-tethered buoys ($r = 0.66$). Periods of missing detections are identified over Hudson Bay, and correlation with MAX-DOAS near-surface columns of BrO (BrO^{200m}) is reduced for both 3σ and 2σ values of BrO^{TH} ($r = 0.54$ and 0.60, respectively). Reducing the statistical threshold in 2012 nearly doubles the calculated emissions with respect to ABr_3σ simulations, demonstrating the sensitivity of these calculations to the removal of the background signal of BrO. While the magnitude of the MAX-DOAS partial columns of BrO is better represented by the ABr_2σ than ABr_3σ scenario, both simulations are poorly correlated with near-surface MAX-DOAS partial columns of BrO.

In 2012, our lower limit estimate of Br_2 emissions, based on the $+3\sigma$ threshold, results in a mean 8% decrease in surface O_3 mixing ratios during April and May months, poleward of 60°N, and isolated decreases in surface O_3 > 25 and 50% over portions of the Arctic. For all years tested, only minor amounts of ozone loss are simulated over the Arctic in March (0.6% in 2012). During April and May 2012, the ABr_2σ emissions result in a mean 20% decrease in surface O_3 with respect to Base simulations. Additionally, with emissions based on the lower threshold for detecting BrO^{TH}, large relative decreases (>50%) in surface O_3 are more frequently simulated over the Arctic Ocean, and mixing ratios of surface layer O_3 are in closer agreement with coastal and buoy observations than in ABr_3σ simulations. However, despite the reduced threshold, only a minor impact on surface O_3 was modeled in March and mixing ratios of O_3 are still biased high with respect to coastal station observations.

The poor agreement with O_3 observations during early spring represents a limitation in our approach, in part due to the emission parameterization underrepresenting BrO^{TH} features in March. However, our method for detecting polar enhancements of Br_y also relies on amplifications in the column of BrO detectable by nadir-viewing satellite instruments, and a lower mass of BrO^{TH} was detected in March than later in the spring. If there are periods where polar emissions produce columns of BrO that are small with respect to the variability in $BrO^{OMI} - BrO^{GC}$ residual, these columns may not be separated from signals originating from the stratosphere or background troposphere. Furthermore, we have identified a case study over Utqiaġvik, Alaska where detection of BrO^{TH} misses elevated mixing ratios of near-surface BrO observed by ground-based instruments during March 2009 (Liao et al., 2011, 2012). These BrO events were associated with stable boundary layer conditions (Boylan et al., 2014), during which satellite instruments are expected to underestimate elevations in near-surface BrO (Peterson et al., 2015; Sihler et al., 2012; Swanson et al., 2020), restricting the use of satellite BrO to validate the model representation of near-surface processes.

While there are anticipated limitations in satellite-based detection of bromine explosion events, BrO^{TH} fields produced by this study with daily coverage of the Arctic are a useful tool to complement instruments that monitor near-surface constituents. Similar satellite-based diagnostics can be produced using GEOS coupled GEOS-Chem

systems under production by the Global Modeling and Assimilation Office, such as from GEOS-CF (v01) which provides near-real time publicly available output, including columns of BrO. The emission fields produced by this study provide an assessment for how much O_3 loss can be explained by the BrO signals, and even with the identified high bias in the ABr_2σ O_3 simulation with respect to coastal stations, there are areas over the Arctic Ocean that experience a 25%–50% reduction in surface O_3 for over half of April and May 2012. Continued development of satellite-based simulations of bromine explosion events leverages the long-term coverage provided by a series of satellite instruments (e.g., Bougoudis et al., 2022) and facilitates comparisons with mechanistic approaches that explicitly represent the production and recycling of brominated species from different polar surfaces.

Overall, our method for implementing polar emissions of Br_2 reproduces the total daily mass of satellite-based hotspots of BrO detected over the Arctic but underestimates local features. A more detailed treatment of the spatial and temporal variability in the lifetime of Br_y is required to represent the satellite-based columns of BrO more accurately. Due to the catalytic nature of bromine-mediated ozone depletion, near-surface ozone simulations are sensitive to how much of BrO^{OMI} is attributed to Arctic Br_2 emissions. The 2σ bias threshold is a likely candidate for future investigations, since the ABr_2σ scenario produced BrO partial columns similar in magnitude to MAX-DOAS lower tropospheric columns. This scenario also increased the frequency of large decreases in surface O_3 over the Arctic Ocean with respect to ABr_3σ but only had a minor impact on surface O_3 during March and over coastal stations. Additionally, the emission scheme presented in this paper relies on a 5-year Base simulation of BrO^{GC} that is mostly of stratospheric origin. More computationally efficient methods for removing the stratospheric signal from satellite-based retrievals of BrO (e.g., Sihler et al., 2012; Theys et al., 2009) would facilitate the incorporation of this emission scheme into long-term historical or near-real time simulations.

Data Availability Statement

The source code for GEOS-Chem v12.0.1 is available at https://zenodo.org/record/1403144 (The International GEOS-Chem Community, 2018). MERRA-2 reanalysis fields (Global Modeling and Assimilation Office, 2015) and OMI data (Chance, 2007) are maintained by the Goddard Earth Sciences Data and Information Services Center (GES DISC). Column measurements of BrO retrieved over Harestua, Norway by UV/Vis Spectroscopy were obtained by Francois Hendrick and Michel Van Roozendael as part of the Network for Detection of Atmospheric Composition Change (NDACC) and are available through the NDACC website (Van Roozendael & Hendrick, n.d.), https://ndacc.larc.nasa.gov/stations/harestua-norway. Measurements of BrO and O_3 collected by instruments onboard autonomous, ice-tethered buoys are maintained by the National Science Foundation (NSF) Arctic Data Center (Simpson et al., 2009). Surface ozone measurements are provided by NOAA for Utqiaġvik (McClure-Begley et al., 2014), the Norwegian Institute for Air Research for the Zeppelin station (Aas & Hjellbrekke, n.d., http://ebas.nilu.no/), and Environment and Climate Change Canada for the Canadian Air and Precipitation Monitoring Network at Alert (Environment and Climate Change Canada, 2017).

Acknowledgments

The authors thank the O-Buoy team for their efforts in the deployment of the instruments onboard ice-tethered buoys and in the collection and analysis of the resulting data. The O-Buoy network was funded by the NSF Office of Polar Programs (OPP). We thank William R. Simpson for his guidance in the usage of BrO measurements collected by MAX-DOAS instruments onboard O-Buoys. We also thank the three anonymous reviewers for their careful reading of the submitted manuscript and helpful comments that contributed to an improved paper. PAW was supported by the NASA Postdoctoral Program, administered by Universities Space Research Association (USRA). Resources supporting the GEOS, coupled with GEOS-Chem, model simulations were provided by the NASA Center for Climate Simulations (NCCS). KEK, CAK, and SP acknowledge support by the NASA Modeling, Analysis and Prediction (MAP) Program (Project manager David Considine).

References

Aas, W., & Hjellbrekke, A. G. (n.d.). Surface ozone collected by UV absorption monitors [Dataset]. Norwegian Institute for Air Research (NILU) EBAS Database. Retrieved from https://ebas.nilu.no/

Ahmed, S., Thomas, J. L., Tuite, K., Stutz, J., Flocke, F., Orlando, J. J., et al. (2022). The role of snow in controlling halogen chemistry and boundary layer oxidation during Arctic spring: A 1D modelling case study. *Journal of Geophysical Research: Atmospheres*, *127*(5), e2021JD036140. https://doi.org/10.1029/2021JD036140

Barrie, L. A., Bottenheim, J. W., Schnell, R. C., Crutzen, P. J., & Rasmussen, R. A. (1988). Ozone destruction and photochemical reactions at polar sunrise in the lower Arctic atmosphere. *Nature*, *334*(6178), 138–141. https://doi.org/10.1038/334138a0

Begoin, M., Richter, A., Weber, M., Kaleschke, L., Tian-Kunze, X., Stohl, A., et al. (2010). Satellite observations of long range transport of a large BrO plume in the Arctic. *Atmospheric Chemistry and Physics*, *10*(14), 6515–6526. https://doi.org/10.5194/acp-10-6515-2010

Benavent, N., Mahajan, A. S., Li, Q., Cuevas, C. A., Schmale, J., Angot, H., et al. (2022). Substantial contribution of iodine to Arctic ozone destruction. *Nature Geoscience*, *15*(10), 770–773. https://doi.org/10.1038/s41561-022-01018-w

Bey, I., Jacob, D. J., Yantosca, R. M., Logan, J. A., Field, B. D., Fiore, A. M., et al. (2001). Global modeling of tropospheric chemistry with assimilated meteorology: Model description and evaluation. *Journal of Geophysical Research*, *106*(D19), 23073–23095. https://doi.org/10.1029/2001JD000807

Blechschmidt, A.-M., Richter, A., Burrows, J. P., Kaleschke, L., Strong, K., Theys, N., et al. (2016). An exemplary case of a bromine explosion event linked to cyclone development in the Arctic. *Atmospheric Chemistry and Physics*, *16*(3), 1773–1788. https://doi.org/10.5194/acp-16-1773-2016

Bloss, W. J., Camredon, M., Lee, J. D., Heard, D. E., Plane, J. M. C., Saiz-Lopez, A., et al. (2010). Coupling of HOx, NOx and halogen chemistry in the Antarctic boundary layer. *Atmospheric Chemistry and Physics*, *10*(21), 10187–10209. https://doi.org/10.5194/acp-10-10187-2010

Bottenheim, J. W., & Chan, E. (2006). A trajectory study into the origin of spring time Arctic boundary layer ozone depletion. *Journal of Geophysical Research*, *111*(D19), D19301. https://doi.org/10.1029/2006JD007055

Bougoudis, I., Blechschmidt, A.-M., Richter, A., Seo, S., & Burrows, J. P. (2022). Simulating tropospheric BrO in the Arctic using an artificial neural network. *Atmospheric Environment*, *276*, 119032. https://doi.org/10.1016/j.atmosenv.2022.119032

Bougoudis, I., Blechschmidt, A.-M., Richter, A., Seo, S., Burrows, J. P., Theys, N., & Rinke, A. (2020). Long-term time series of Arctic tropospheric BrO derived from UV–VIS satellite remote sensing and its relation to first-year sea ice. *Atmospheric Chemistry and Physics*, *20*(20), 11869–11892. https://doi.org/10.5194/acp-20-11869-2020

Boylan, P., Helmig, D., Staebler, R., Turnipseed, A., Fairall, C., & Neff, W. (2014). Boundary layer dynamics during the Ocean-Atmosphere-Sea-Ice-Snow (OASIS) 2009 experiment at Barrow, AK: Boundary layer dynamics during oasis. *Journal of Geophysical Research: Atmospheres*, *119*(5), 2261–2278. https://doi.org/10.1002/2013JD020299

Bucsela, E. J., Krotkov, N. A., Celarier, E. A., Lamsal, L. N., Swartz, W. H., Bhartia, P. K., et al. (2013). A new stratospheric and tropospheric NO_2 retrieval algorithm for nadir-viewing satellite instruments: Applications to OMI. *Atmospheric Measurement Techniques*, *6*(10), 2607–2626. https://doi.org/10.5194/amt-6-2607-2013

Burd, J. A., Peterson, P. K., Nghiem, S. V., Perovich, D. K., & Simpson, W. R. (2017). Snow melt onset hinders bromine monoxide heterogeneous recycling in the Arctic. *Submitted to Journal of Geophysical Research: Atmospheres*, *122*(15), 8297–8309. https://doi.org/10.1002/2017JD026906

Burkholder, J. B., Sander, S. P., Abbatt, J., Barker, J. R., Huie, R. E., Kolb, C. E., et al. (2015). *Chemical kinetics and photochemical data for use in atmospheric studies, Evaluation Number 18*. Jet Propulsion Laboratory. Retrieved from http://jpldataeval.jpl.nasa.gov/

Cao, L., Sihler, H., Platt, U., & Gutheil, E. (2014). Numerical analysis of the chemical kinetic mechanisms of ozone depletion and halogen release in the polar troposphere. *Atmospheric Chemistry and Physics*, *14*(7), 3771–3787. https://doi.org/10.5194/acp-14-3771-2014

Carlson, D., Donohoue, D., Platt, U., & Simpson, W. R. (2010). A low power automated MAX-DOAS instrument for the Arctic and other remote unmanned locations. *Atmospheric Measurement Techniques*, *3*(2), 429–439. https://doi.org/10.5194/amt-3-429-2010

Carpenter, L. J., Daniel, J. S., Fleming, E. L., Hanaoka, T., Hu, J., Ravishankara, A. R., et al. (2018). Scenarios and information for policymakers, Chapter 6. In *Scientific assessment of ozone depletion: 2018*. World Meteorological Organization.

Chance, K. (1998). Analysis of BrO measurements from the Global Ozone Monitoring Experiment. *Geophysical Research Letters*, *25*(17), 3335–3338. https://doi.org/10.1029/98GL52359

Chance, K. (2007). OMI/Aura bromine monoxide (BrO) total column 1-orbit L2 Swath 13x24 km [Dataset]. NASA Goddard Earth Sciences Data and Information Services Center. https://doi.org/10.5067/AURA/OMI/DATA2006

Chen, Q., Schmidt, J. A., Shah, V., Jaeglé, L., Sherwen, T., & Alexander, B. (2017). Sulfate production by reactive bromine: Implications for the global sulfur and reactive bromine budgets. *Geophysical Research Letters*, *44*(13), 7069–7078. https://doi.org/10.1002/2017GL073812

Choi, S., Theys, N., Salawitch, R. J., Wales, P. A., Joiner, J., Canty, T. P., et al. (2018). Link between Arctic tropospheric BrO explosion observed from space and sea-salt aerosols from blowing snow investigated using ozone monitoring instrument BrO data and GEOS-5 data assimilation system. *Journal of Geophysical Research: Atmospheres*, *123*(13), 6954–6983. https://doi.org/10.1029/2017JD026889

Choi, S., Wang, Y., Salawitch, R. J., Canty, T., Joiner, J., Zeng, T., et al. (2012). Analysis of satellite-derived Arctic tropospheric BrO columns in conjunction with aircraft measurements during ARCTAS and ARCPAC. *Atmospheric Chemistry and Physics*, *12*(3), 1255–1285. https://doi.org/10.5194/acp-12-1255-2012

Custard, K. D., Raso, A. R. W., Shepson, P. B., Staebler, R. M., & Pratt, K. A. (2017). Production and release of molecular bromine and chlorine from the Arctic coastal snowpack. *ACS Earth and Space Chemistry*, *1*(3), 142–151. https://doi.org/10.1021/acsearthspacechem.7b00014

Domine, F., Sparapani, R., Ianniello, A., & Beine, H. J. (2004). The origin of sea salt in snow on Arctic sea ice and in coastal regions. *Atmospheric Chemistry and Physics*, *4*(9/10), 2259–2271. https://doi.org/10.5194/acp-4-2259-2004

Douglass, A. R., Stolarski, R. S., Strahan, S. E., & Connell, P. S. (2004). Radicals and reservoirs in the GMI chemistry and transport model: Comparison to measurements. *Journal of Geophysical Research*, *109*(D16), D16302. https://doi.org/10.1029/2004JD004632

Eastham, S. D., Weisenstein, D. K., & Barrett, S. R. H. (2014). Development and evaluation of the unified tropospheric-stratospheric chemistry extension (UCX) for the global chemistry-transport model GEOS-Chem. *Atmospheric Environment*, *89*, 52–63. https://doi.org/10.1016/j.atmosenv.2014.02.001

Engel, A., Rigby, M., Burkholder, J. B., Fernandez, R. P., Froidevaux, L., Hall, B. D., et al. (2018). Update on ozone-depleting substances (ODSs) and other gases of interest to the Montreal protocol, Chapter 1. In *Scientific assessment of ozone depletion: 2018, Global ozone research and monitoring project – Report No. 58*. World Meteorological Organization.

Environment and Climate Change Canada. (2017). Canadian air and precipitation monitoring network (CAPMoN) monitoring of atmospheric gases and ground level ozone [Dataset]. Toronto, Ontario, Canada at open.canada.ca: Government of Canada Open Data Portal. Retrieved from https://donnees.ec.gc.ca/data/air/monitor/monitoring-of-atmospheric-gases/ground-level-ozone/

Evans, M. J., Jacob, D. J., Atlas, E., Cantrell, C. A., Eisele, F., Flocke, F., et al. (2003). Coupled evolution of BrO_x -ClO_x -HO_x -NO_x chemistry during bromine-catalyzed ozone depletion events in the arctic boundary layer. *Journal of Geophysical Research*, *108*(D4), 8368. https://doi.org/10.1029/2002JD002732

Falk, S., & Sinnhuber, B. M. (2018). Polar boundary layer bromine explosion and ozone depletion events in the chemistry-climate model EMAC v2.52: Implementation and evaluation of AirSnow algorithm. *Geoscientific Model Development*, *11*(3), 1115–1131. https://doi.org/10.5194/gmd-11-1115-2018

Fan, S.-M., & Jacob, D. J. (1992). Surface ozone depletion in Arctic spring sustained by bromine reactions on aerosols. *Nature*, *359*(6395), 522–524. https://doi.org/10.1038/359522a0

Fernandez, R. P., Carmona-Balea, A., Cuevas, C. A., Barrera, J. A., Kinnison, D. E., Lamarque, J., et al. (2019). Modeling the sources and chemistry of polar tropospheric halogens (Cl, Br, and I) using the CAM-Chem global chemistry-climate model. *Journal of Advances in Modeling Earth Systems*, *11*(7), 2259–2289. https://doi.org/10.1029/2019MS001655

Finlayson-Pitts, B. J. (2010). Halogens in the troposphere. *Analytical Chemistry*, *82*(3), 770–776. https://doi.org/10.1021/ac901478p

Fleischmann, O. C., Hartmann, M., Burrows, J. P., & Orphal, J. (2004). New ultraviolet absorption cross-sections of BrO at atmospheric temperatures measured by time-windowing Fourier transform spectroscopy. *Journal of Photochemistry and Photobiology A: Chemistry*, *168*(1–2), 117–132. https://doi.org/10.1016/j.jphotochem.2004.03.026

Foster, K. L., Plastridge, R. A., Bottenheim, J. W., Shepson, P. B., Finlayson-Pitts, B. J., & Spicer, C. W. (2001). The role of Br_2 and BrCl in surface ozone destruction at polar sunrise. *Science*, *291*(5503), 471–474. https://doi.org/10.1126/science.291.5503.471

Frey, M. M., Norris, S. J., Brooks, I. M., Anderson, P. S., Nishimura, K., Yang, X., et al. (2020). First direct observation of sea salt aerosol production from blowing snow above sea ice. *Atmospheric Chemistry and Physics*, *20*(4), 2549–2578. https://doi.org/10.5194/acp-20-2549-2020

Frieß, U., Hollwedel, J., König-Langlo, G., Wagner, T., & Platt, U. (2004). Dynamics and chemistry of tropospheric bromine explosion events in the Antarctic coastal region. *Journal of Geophysical Research*, *109*(D6), n/a. https://doi.org/10.1029/2003JD004133

Frieß, U., Monks, P. S., Remedios, J. J., Rozanov, A., Sinreich, R., Wagner, T., & Platt, U. (2006). MAX-DOAS O_4 measurements: A new technique to derive information on atmospheric aerosols: 2. Modeling studies. *Journal of Geophysical Research*, *111*(D14), D14203. https://doi.org/10.1029/2005JD006618

Frieß, U., Sihler, H., Sander, R., Pöhler, D., Yilmaz, S., & Platt, U. (2011). The vertical distribution of BrO and aerosols in the Arctic: Measurements by active and passive differential optical absorption spectroscopy. *Journal of Geophysical Research*, *116*(18), D00R04. https://doi.org/10.1029/2011JD015938

Gao, Z., Geilfus, N.-X., Saiz-Lopez, A., & Wang, F. (2022). Reproducing Arctic springtime tropospheric ozone and mercury depletion events in an outdoor mesocosm sea ice facility. *Atmospheric Chemistry and Physics*, *22*(3), 1811–1824. https://doi.org/10.5194/acp-22-1811-2022

Gelaro, R., McCarty, W., Suárez, M. J., Todling, R., Molod, A., Takacs, L., et al. (2017). The modern-era retrospective analysis for research and applications, Version 2 (MERRA-2). *Journal of Climate*, *30*(14), 5419–5454. https://doi.org/10.1175/JCLI-D-16-0758.1

Global Modeling and Assimilation Office. (2015). MERRA-2 tavg3_3d_asm_Nv: 3d, 3-hourly, time-averaged, model-level, assimilation, assimilated meteorological fields V5.12.4 [Dataset]. NASA Goddard Earth Sciences Data and Information Services Center. https://doi.org/10.5067/SUOQESM06LPK

Halfacre, J. W., Knepp, T. N., Shepson, P. B., Thompson, C. R., Pratt, K. A., Li, B., et al. (2014). Temporal and spatial characteristics of ozone depletion events from measurements in the Arctic. *Atmospheric Chemistry and Physics*, *14*(10), 4875–4894. https://doi.org/10.5194/acp-14-4875-2014

Hendrick, F., Rozanov, A., Johnston, P. V., Bovensmann, H., De Mazière, M., Fayt, C., et al. (2009). Multi-year comparison of stratospheric BrO vertical profiles retrieved from SCIAMACHY limb and ground-based UV-visible measurements. *Atmospheric Measurement Techniques*, *2*(1), 273–285. https://doi.org/10.5194/amt-2-273-2009

Hendrick, F., Van Roozendael, M., Chipperfield, M. P., Dorf, M., Goutail, F., Yang, X., et al. (2007). Retrieval of stratospheric and tropospheric BrO profiles and columns using ground-based zenith-sky DOAS observations at Harestua, 60° N. *Atmospheric Chemistry and Physics*, *7*(18), 4869–4885. https://doi.org/10.5194/acp-7-4869-2007

Herrmann, M., Sihler, H., Frieß, U., Wagner, T., Platt, U., & Gutheil, E. (2021). Time-dependent 3D simulations of tropospheric ozone depletion events in the Arctic spring using the weather research and forecasting model coupled with Chemistry (WRF-Chem). *Atmospheric Chemistry and Physics*, *21*(10), 7611–7638. https://doi.org/10.5194/acp-21-7611-2021

Hollwedel, J., Wenig, M., Beirle, S., Kraus, S., Kuhl, S., Wilms-Grabe, W., et al. (2004). Year-to-year variations of spring time polar tropospheric BrO as seen by GOME. *Advances in Space Research*, *34*(4), 804–808. https://doi.org/10.1016/j.asr.2003.08.060

Holmes, C. D., Jacob, D. J., & Yang, X. (2006). Global lifetime of elemental mercury against oxidation by atomic bromine in the free troposphere. *Geophysical Research Letters*, *33*(20), L20808. https://doi.org/10.1029/2006GL027176

Hu, L., Keller, C. A., Long, M. S., Sherwen, T., Auer, B., Da Silva, A., et al. (2018). Global simulation of tropospheric chemistry at 12.5 km resolution: Performance and evaluation of the GEOS-Chem chemical module (v10-1) within the NASA GEOS Earth system model (GEOS-5 ESM). *Geoscientific Model Development*, *11*(11), 4603–4620. https://doi.org/10.5194/gmd-11-4603-2018

Huang, J., Jaeglé, L., Chen, Q., Alexander, B., Sherwen, T., Evans, M. J., et al. (2020). Evaluating the impact of blowing-snow sea salt aerosol on springtime BrO and O_3 in the Arctic. *Atmospheric Chemistry and Physics*, *20*(12), 7335–7358. https://doi.org/10.5194/acp-20-7335-2020

Huang, J., Jaeglé, L., & Shah, V. (2018). Using CALIOP to constrain blowing snow emissions of sea salt aerosols over Arctic and Antarctic sea ice. *Atmospheric Chemistry and Physics*, *18*(22), 16253–16269. https://doi.org/10.5194/acp-18-16253-2018

Jeong, D., McNamara, S. M., Barget, A. J., Raso, A. R. W., Upchurch, L. M., Thanekar, S., et al. (2022). Multiphase reactive bromine chemistry during late spring in the Arctic: Measurements of gases, particles, and snow. *ACS Earth and Space Chemistry*, *6*(12), 2877–2887. https://doi.org/10.1021/acsearthspacechem.2c00189

Jones, A. E., Anderson, P. S., Begoin, M., Brough, N., Hutterli, M. A., Marshall, G. J., et al. (2009). BrO, blizzards, and drivers of polar tropospheric ozone depletion events. *Atmospheric Chemistry and Physics*, *9*(14), 4639–4652. https://doi.org/10.5194/acp-9-4639-2009

Jones, A. E., Anderson, P. S., Wolff, E. W., Turner, J., Rankin, A. M., & Colwell, S. R. (2006). A role for newly forming sea ice in springtime polar tropospheric ozone loss? Observational evidence from Halley station, Antarctica. *Journal of Geophysical Research*, *111*(D8), D08306. https://doi.org/10.1029/2005JD006566

Keil, A. D., & Shepson, P. B. (2006). Chlorine and bromine atom ratios in the springtime Arctic troposphere as determined from measurements of halogenated volatile organic compounds. *Journal of Geophysical Research*, *111*(D17), D17303. https://doi.org/10.1029/2006JD007119

Keller, C. A., Knowland, K. E., Duncan, B. N., Liu, J., Anderson, D. C., Das, S., et al. (2021). Description of the NASA GEOS Composition Forecast Modeling System GEOS-CF v1.0. *Journal of Advances in Modeling Earth Systems*, *13*(4), e2020MS002413. https://doi.org/10.1029/2020MS002413

Keller, C. A., Long, M. S., Yantosca, R. M., Da Silva, A. M., Pawson, S., & Jacob, D. J. (2014). HEMCO v1.0: A versatile, ESMF-compliant component for calculating emissions in atmospheric models. *Geoscientific Model Development*, *7*(4), 1409–1417. https://doi.org/10.5194/gmd-7-1409-2014

Knepp, T. N., Bottenheim, J., Carlsen, M., Carlson, D., Donohoue, D., Friederich, G., et al. (2010). Development of an autonomous sea ice tethered buoy for the study of ocean-atmosphere-sea ice-snow pack interactions: The O-buoy. *Atmospheric Measurement Techniques*, *3*(1), 249–261. https://doi.org/10.5194/amt-3-249-2010

Knowland, K. E., Keller, C. A., Wales, P. A., Wargan, K., Coy, L., Johnson, M. S., et al. (2022). NASA GEOS composition forecast modeling system GEOS-CF v1.0: Stratospheric composition. *Journal of Advances in Modeling Earth Systems*, *14*(6), e2021MS002852. https://doi.org/10.1029/2021MS002852

Krotkov, N. A., Lamsal, L. N., Celarier, E. A., Swartz, W. H., Marchenko, S. V., Bucsela, E. J., et al. (2017). The version 3 OMI NO_2 standard product. *Atmospheric Measurement Techniques*, *10*(9), 3133–3149. https://doi.org/10.5194/amt-10-3133-2017

Levelt, P. F., Van den Oord, G. H. J., Dobber, M. R., Malkki, A., Visser, H., de Vries, J., et al. (2006). The ozone monitoring instrument. *IEEE Transactions on Geoscience and Remote Sensing*, *44*(5), 1093–1101. Urn:nbn:nl:ui:25-648485. https://doi.org/10.1109/tgrs.2006.872333

Liao, J., Huey, L. G., Liu, Z., Tanner, D. J., Cantrell, C. A., Orlando, J. J., et al. (2014). High levels of molecular chlorine in the Arctic atmosphere. *Nature Geoscience*, *7*(2), 91–94. https://doi.org/10.1038/ngeo2046

Liao, J., Huey, L. G., Tanner, D. J., Flocke, F. M., Orlando, J. J., Neuman, J. A., et al. (2012). Observations of inorganic bromine (HOBr, BrO, and Br_2) speciation at Barrow, Alaska, in spring 2009. *Journal of Geophysical Research*, *117*(6), 1–12. https://doi.org/10.1029/2011JD016641

Liao, J., Sihler, H., Huey, L. G., Neuman, J. A., Tanner, D. J., Friess, U., et al. (2011). A comparison of Arctic BrO measurements by chemical ionization mass spectrometry and long path-differential optical absorption spectroscopy. *Journal of Geophysical Research*, *116*(1), 1–14. https://doi.org/10.1029/2010JD014788

Long, M. S., Yantosca, R., Nielsen, J. E., Keller, C. A., da Silva, A., Sulprizio, M. P., et al. (2015). Development of a grid-independent GEOS-Chem chemical transport model (v9-02) as an atmospheric chemistry module for Earth system models. *Geoscientific Model Development*, *8*(3), 595–602. https://doi.org/10.5194/gmd-8-595-2015

Mahajan, A. S., Shaw, M., Oetjen, H., Hornsby, K. E., Carpenter, L. J., Kaleschke, L., et al. (2010). Evidence of reactive iodine chemistry in the Arctic boundary layer. *Journal of Geophysical Research*, *115*(D20), D20303. https://doi.org/10.1029/2009JD013665

Marelle, L., Thomas, J. L., Ahmed, S., Tuite, K., Stutz, J., Dommergue, A., et al. (2021). Implementation and impacts of surface and blowing snow sources of Arctic bromine activation within WRF-Chem 4.1.1. *Journal of Advances in Modeling Earth Systems*, *13*(8), e2020MS002391. https://doi.org/10.1029/2020MS002391

McClure-Begley, A., Petropavlovskikh, I., & Oltmans, S. (2014). NOAA Global Monitoring Surface Ozone Network [Dataset]. NOAA Earth Systems Research Laboratory Global Monitoring Division. http://dx.doi.org/10.7289/V57P8WBF

McPeters, R., Kroon, M., Labow, G., Brinksma, E., Balis, D., Petropavlovskikh, I., et al. (2008). Validation of the aura ozone monitoring instrument total column ozone product. *Journal of Geophysical Research*, *113*(D15), D15S14. https://doi.org/10.1029/2007JD008802

Molod, A., Takacs, L., Suarez, M., & Bacmeister, J. (2015). Development of the GEOS-5 atmospheric general circulation model: Evolution from MERRA to MERRA2. *Geoscientific Model Development*, *8*(5), 1339–1356. https://doi.org/10.5194/gmd-8-1339-2015

Nielsen, J. E., Pawson, S., Molod, A., Auer, B., da Silva, A. M., Douglass, A. R., et al. (2017). Chemical mechanisms and their applications in the Goddard earth observing system (GEOS) earth system model. *Journal of Advances in Modeling Earth Systems*, *9*(8), 3019–3044. https://doi.org/10.1002/2017MS001011

Oltmans, S. J., & Levy, H. (1994). Surface ozone measurements from a global network. *Atmospheric Environment*, *28*(1), 9–24. https://doi.org/10.1016/1352-2310(94)90019-1

Oltmans, S. J., Schnell, R. C., Sheridan, P. J., Perterson, R. E., Li, S.-M., Winchester, J. W., et al. (1989). Seasonal surface ozone and filterable bromine relationship in the high Artic. *Atmospheric Environment*, *23*(11), 2431–2441. https://doi.org/10.1016/0004-6981(89)90254-0

Orbe, C., Oman, L. D., Strahan, S. E., Waugh, D. W., Pawson, S., Takacs, L. L., & Molod, A. M. (2017). Large-scale atmospheric transport in GEOS replay simulations. *Journal of Advances in Modeling Earth Systems*, *9*(7), 2545–2560. https://doi.org/10.1002/2017MS001053

Peterson, P. K., Pöhler, D., Sihler, H., Zielcke, J., General, S., Frieß, U., et al. (2017). Observations of bromine monoxide transport in the Arctic sustained on aerosol particles. *Atmospheric Chemistry and Physics*, *17*(12), 7567–7579. https://doi.org/10.5194/acp-17-7567-2017

Peterson, P. K., Pöhler, D., Zielcke, J., General, S., Frieß, U., Platt, U., et al. (2018). Springtime bromine activation over coastal and Inland Arctic snowpacks. *ACS Earth and Space Chemistry*, *2*(10), 1075–1086. https://doi.org/10.1021/acsearthspacechem.8b00083

Peterson, P. K., Simpson, W. R., Pratt, K. A., Shepson, P. B., Frieß, U., Zielcke, J., et al. (2015). Dependence of the vertical distribution of bromine monoxide in the lower troposphere on meteorological factors such as wind speed and stability. *Atmospheric Chemistry and Physics*, *15*(4), 2119–2137. https://doi.org/10.5194/acp-15-2119-2015

Platt, S. M., Hov, Ø., Berg, T., Breivik, K., Eckhardt, S., Eleftheriadis, K., et al. (2022). Atmospheric composition in the European Arctic and 30 years of the Zeppelin Observatory, Ny-Ålesund. *Atmospheric Chemistry and Physics*, *22*(5), 3321–3369. https://doi.org/10.5194/acp-22-3321-2022

Platt, U., & Stutz, J. (2008). Differential optical absorption spectroscopy.

Pratt, K. A. (2019). Tropospheric halogen photochemistry in the rapidly changing Arctic. *Trends in Chemistry*, *1*(6), 545–548. https://doi.org/10.1016/j.trechm.2019.06.001

Pratt, K. A., Custard, K. D., Shepson, P. B., Douglas, T. A., Pöhler, D., General, S., et al. (2013). Photochemical production of molecular bromine in Arctic surface snowpacks. *Nature Geoscience*, *6*(5), 351–356. https://doi.org/10.1038/ngeo1779

Raso, A. R. W., Custard, K. D., May, N. W., Tanner, D., Newburn, M. K., Walker, L., et al. (2017). Active molecular iodine photochemistry in the Arctic. *Proceedings of the National Academy of Sciences*, *114*(38), 10053–10058. https://doi.org/10.1073/pnas.1702803114

Richter, A., Wittrock, F., Eisinger, M., & Burrows, J. P. (1998). GOME observations of tropospheric BrO in northern hemispheric spring and summer 1997. *Geophysical Research Letters*, *25*(14), 2683–2686. https://doi.org/10.1029/98GL52016

Rodgers, C. D. (2000). *Inverse methods for atmospheric sounding: Theory and practice*. World Scientific.

Saiz-Lopez, A., Plane, J. M. C., Baker, A. R., Carpenter, L. J., von Glasow, R., Gómez Martín, J. C., et al. (2012). Atmospheric chemistry of iodine. *Chemical Reviews*, *112*(3), 1773–1804. https://doi.org/10.1021/cr200029u

Saiz-Lopez, A., & von Glasow, R. (2012). Reactive halogen chemistry in the troposphere. *Chemical Society Reviews*, *41*(19), 6448. https://doi.org/10.1039/c2cs35208g

Salawitch, R. J., Canty, T., Kurosu, T., Chance, K., Liang, Q., Da Silva, A., et al. (2010). A new interpretation of total column BrO during Arctic spring. *Geophysical Research Letters*, *37*(21), 1–9. https://doi.org/10.1029/2010GL043798

Schenkeveld, V. M. E., Jaross, G., Marchenko, S., Haffner, D., Kleipool, Q. L., Rozemeijer, N. C., et al. (2017). In-flight performance of the ozone monitoring instrument. *Atmospheric Measurement Techniques*, *10*(5), 1957–1986. https://doi.org/10.5194/amt-10-1957-2017

Schmidt, J. A., Jacob, D. J., Horowitz, H. M., Hu, L., Sherwen, T., Evans, M. J., et al. (2016). Modeling the observed tropospheric BrO background: Importance of multiphase chemistry and implications for ozone, OH, and mercury. *Journal of Geophysical Research: Atmospheres*, *121*(19), 11819–11835. https://doi.org/10.1002/2015JD024229

Schofield, R., Kreher, K., Conner, B. J., Johnston, P. V., Thomas, A., Shooter, D., et al. (2004). Retrieved tropospheric and stratospheric BrO columns over Lauder, New Zealand. *Journal of Geophysical Research*, *109*(D14), D14304. https://doi.org/10.1029/2003JD004463

Schroeder, W. H., Anlauf, K. G., Barrie, L. A., Lu, J. Y., Steffen, A., Schneeberger, D. R., & Berg, T. (1998). Arctic springtime depletion of mercury. *Nature*, *394*(6691), 331–332. https://doi.org/10.1038/28530

Seo, S., Richter, A., Blechschmidt, A.-M., Bougoudis, I., & Burrows, J. P. (2019). First high-resolution BrO column retrievals from TROPOMI. *Atmospheric Measurement Techniques*, *12*(5), 2913–2932. https://doi.org/10.5194/amt-12-2913-2019

Seo, S., Richter, A., Blechschmidt, A.-M., Bougoudis, I., & Burrows, J. P. (2020). Spatial distribution of enhanced BrO and its relation to meteorological parameters in Arctic and Antarctic Sea ice regions. *Atmospheric Chemistry and Physics*, *20*(20), 12285–12312. https://doi.org/10.5194/acp-20-12285-2020

Sherwen, T., Evans, M. J., Carpenter, L. J., Andrews, S. J., Lidster, R. T., Dix, B., et al. (2016a). Iodine's impact on tropospheric oxidants: A global model study in GEOS-Chem. *Atmospheric Chemistry and Physics*, *16*(2), 1161–1186. https://doi.org/10.5194/acp-16-1161-2016

Sherwen, T., Schmidt, J. A., Evans, M. J., Carpenter, L. J., Großmann, K., Eastham, S. D., et al. (2016b). Global impacts of tropospheric halogens (Cl, Br, I) on oxidants and composition in GEOS-Chem. *Atmospheric Chemistry and Physics*, *16*(18), 12239–12271. https://doi.org/10.5194/acp-16-12239-2016

Sihler, H., Platt, U., Beirle, S., Marbach, T., Kühl, S., Dörner, S., et al. (2012). Tropospheric BrO column densities in the Arctic derived from satellite: Retrieval and comparison to ground-based measurements. *Atmospheric Measurement Techniques*, *5*(11), 2779–2807. https://doi.org/10.5194/amt-5-2779-2012

Simpson, W. R., Alvarez-Aviles, L., Douglas, T. A., Sturm, M., & Domine, F. (2005). Halogens in the coastal snow pack near Barrow, Alaska: Evidence for active bromine air-snow chemistry during springtime: Bromide in snow near barrow. *Geophysical Research Letters*, *32*(4), n/a. https://doi.org/10.1029/2004GL021748

Simpson, W. R., Brown, S. S., Saiz-Lopez, A., Thornton, J. A., & Von Glasow, R. (2015). Tropospheric halogen chemistry: Sources, cycling, and impacts. *Chemical Reviews*, *115*(10), 4035–4062. https://doi.org/10.1021/cr5006638

Simpson, W. R., Perovich, D., Matrai, P., Shepson, P., & Chavez, F. (2009). The collaborative O-Buoy project: Deployment of a network of Arctic Ocean chemical sensors for the IPY and beyond [Dataset]. *Arctic Data Center*. https://doi.org/10.18739/A2WD4W

Simpson, W. R., Peterson, P. K., Frieß, U., Sihler, H., Lampel, J., Platt, U., et al. (2017). Horizontal and vertical structure of reactive bromine events probed by bromine monoxide MAX-DOAS. *Atmospheric Chemistry and Physics*, *17*(15), 9291–9309. https://doi.org/10.5194/acp-17-9291-2017

Simpson, W. R., von Glasow, R., Riedel, K., Anderson, P., Ariya, P., Bottenheim, J., et al. (2007). Halogens and their role in polar boundary-layer ozone depletion. *Atmospheric Chemistry and Physics*, *7*(16), 4375–4418. https://doi.org/10.5194/acp-7-4375-2007

Sioris, C. E., Kovalenko, L. J., McLinden, C. A., Salawitch, R. J., Van Roozendael, M., Goutail, F., et al. (2006). Latitudinal and vertical distribution of bromine monoxide in the lower stratosphere from scanning imaging absorption spectrometer for atmospheric chartography limb scattering measurements. *Journal of Geophysical Research*, *111*(D14), D14301. https://doi.org/10.1029/2005JD006479

Spurr, R. J. D., Kurosu, T. P., & Chance, K. V. (2001). A linearized discrete ordinate radiative transfer model for atmospheric remote-sensing retrieval. *Journal of Quantitative Spectroscopy and Radiative Transfer*, *68*(6), 689–735. https://doi.org/10.1016/S0022-4073(00)00055-8

Stephens, C. R., Shepson, P. B., Steffen, A., Bottenheim, J. W., Liao, J., Huey, L. G., et al. (2012). The relative importance of chlorine and bromine radicals in the oxidation of atmospheric mercury at Barrow, Alaska: Mercury oxidation in the Arctic. *Journal of Geophysical Research*, *117*(D14), n/a. https://doi.org/10.1029/2011JD016649

Strahan, S. E., Duncan, B. N., & Hoor, P. (2007). Observationally derived transport diagnostics for the lowermost stratosphere and their application to the GMI chemistry and transport model. *Atmospheric Chemistry and Physics*, *7*, 2435–2445. https://doi.org/10.5194/acpd-7-1449-2007

Suleiman, R. M., Chance, K., Liu, X., González Abad, G., Kurosu, T. P., Hendrick, F., & Theys, N. (2019). OMI total bromine monoxide (OMBRO) data product: Algorithm, retrieval and measurement comparisons. *Atmospheric Measurement Techniques*, *12*(4), 2067–2084. https://doi.org/10.5194/amt-12-2067-2019

Swanson, W. F., Graham, K. A., Halfacre, J. W., Holmes, C. D., Shepson, P. B., & Simpson, W. R. (2020). Arctic reactive bromine events occur in two distinct sets of environmental conditions: A statistical analysis of 6 years of observations. *Journal of Geophysical Research: Atmospheres*, *125*(10), e2019JD032139. https://doi.org/10.1029/2019JD032139

Swanson, W. F., Holmes, C. D., Simpson, W. R., Confer, K., Marelle, L., Thomas, J. L., et al. (2022). Comparison of model and ground observations finds snowpack and blowing snow aerosols both contribute to Arctic tropospheric reactive bromine. *Atmospheric Chemistry and Physics*, *22*(22), 14467–14488. https://doi.org/10.5194/acp-22-14467-2022

The International GEOS-Chem Community. (2018). geoschem/geos-chem: GEOS-Chem 12.0.1 release. *Zenodo*. https://doi.org/10.5281/ZENODO.1403144

Theys, N., Van Roozendael, M., Errera, Q., Hendrick, F., Daerden, F., Chabrillat, S., et al. (2009). A global stratospheric bromine monoxide climatology based on the BASCOE chemical transport model. *Atmospheric Chemistry and Physics*, *9*(3), 831–848. https://doi.org/10.5194/acp-9-831-2009

Theys, N., Van Roozendael, M., Hendrick, F., Yang, X., De Smedt, I., Richter, A., et al. (2011). Global observations of tropospheric BrO columns using GOME-2 satellite data. *Atmospheric Chemistry and Physics*, *11*(4), 1791–1811. https://doi.org/10.5194/acp-11-1791-2011

Thompson, C. R., Shepson, P. B., Liao, J., Huey, L. G., Apel, E. C., Cantrell, C. A., et al. (2015). Interactions of bromine, chlorine, and iodine photochemistry during ozone depletions in Barrow, Alaska. *Atmospheric Chemistry and Physics*, *15*(16), 9651–9679. https://doi.org/10.5194/acp-15-9651-2015

Thompson, C. R., Shepson, P. B., Liao, J., Huey, L. G., Cantrell, C., Flocke, F., & Orlando, J. (2017). Bromine atom production and chain propagation during springtime Arctic ozone depletion events in Barrow, Alaska. *Atmospheric Chemistry and Physics*, *17*(5), 3401–3421. https://doi.org/10.5194/acp-17-3401-2017

Tørseth, K., Aas, W., Breivik, K., Fjæraa, A. M., Fiebig, M., Hjellbrekke, A. G., et al. (2012). Introduction to the European Monitoring and Evaluation Programme (EMEP) and observed atmospheric composition change during 1972–2009. *Atmospheric Chemistry and Physics*, *12*(12), 5447–5481. https://doi.org/10.5194/acp-12-5447-2012

Toyota, K., McConnell, J. C., Lupu, A., Neary, L., McLinden, C. A., Richter, A., et al. (2011). Analysis of reactive bromine production and ozone depletion in the Arctic boundary layer using 3-D simulations with GEM-AQ: Inference from synoptic-scale patterns. *Atmospheric Chemistry and Physics*, *11*(8), 3949–3979. https://doi.org/10.5194/acp-11-3949-2011

Van Roozendael, M., & Hendrick, F. (n.d.). UV/Visible Spectrometer Measurements of BrO at the Harestua, Norway Station (Version 100) [Dataset]. Network for the Detection of Atmospheric Composition Change (NDACC). Retrieved from https://ndacc.larc.nasa.gov/stations/harestua-norway

Van Roozendael, M., Wagner, T., Richter, A., Pundt, I., Arlander, D. W., Burrows, J. P., et al. (2002). Intercomparison of BrO measurements from ERS-2 GOME, ground-based and balloon platforms. *Advances in Space Research*, *29*(11), 1661–1666. https://doi.org/10.1016/S0273-1177(02)00098-4

Vasilkov, A., Joiner, J., Haffner, D., Bhartia, P. K., & Spurr, R. J. D. (2010). What do satellite backscatter ultraviolet and visible spectrometers see over snow and ice? A study of clouds and ozone using the A-train. *Atmospheric Measurement Techniques*, *3*(3), 619–629. https://doi.org/10.5194/amt-3-619-2010

Vasilkov, A., Joiner, J., Spurr, R., Bhartia, P. K., Levelt, P., & Stephens, G. (2008). Evaluation of the OMI cloud pressures derived from rotational Raman scattering by comparisons with other satellite data and radiative transfer simulations. *Journal of Geophysical Research*, *113*(D15), D15S19. https://doi.org/10.1029/2007JD008689

Wagner, T., & Platt, U. (1998). Satellite mapping of enhanced BrO concentrations in the troposphere. *Nature*, *395*(6701), 486–490. https://doi.org/10.1038/26723

Wales, P. A., Salawitch, R. J., Lind, E. S., Mount, G. H., Canty, T. P., Chance, K., et al. (2021). Evaluation of the stratospheric and tropospheric bromine burden over Fairbanks, Alaska based on column retrievals of bromine monoxide. *Journal of Geophysical Research: Atmospheres*, *126*(2), e2020JD032896. https://doi.org/10.1029/2020JD032896

Wang, S., McNamara, S. M., Moore, C. W., Obrist, D., Steffen, A., Shepson, P. B., et al. (2019a). Direct detection of atmospheric atomic bromine leading to mercury and ozone depletion. *Proceedings of the National Academy of Sciences*, *116*(29), 14479–14484. https://doi.org/10.1073/pnas.1900613116

Wang, S., & Pratt, K. A. (2017). Molecular halogens above the Arctic snowpack: Emissions, diurnal variations, and recycling mechanisms. *Journal of Geophysical Research: Atmospheres*, *122*(21), 11991–12007. https://doi.org/10.1002/2017JD027175

Wang, X., Jacob, D. J., Downs, W., Zhai, S., Zhu, L., Shah, V., et al. (2021). Global tropospheric halogen (Cl, Br, I) chemistry and its impact on oxidants. *Atmospheric Chemistry and Physics*, *21*(18), 13973–13996. https://doi.org/10.5194/acp-21-13973-2021

Wang, X., Jacob, D. J., Eastham, S. D., Sulprizio, M. P., Zhu, L., Chen, Q., et al. (2019b). The role of chlorine in global tropospheric chemistry. *Atmospheric Chemistry and Physics*, *19*(6), 3981–4003. https://doi.org/10.5194/acp-19-3981-2019

Wennberg, P. (1999). Bromine explosion. *Nature*, *397*(6717), 299–301. https://doi.org/10.1038/16805

Wessel, S., Aoki, S., Winkler, P., Weller, R., Herber, A., Gernandt, H., & Schrems, O. (1998). Tropospheric ozone depletion in polar regions A comparison of observations in the Arctic and Antarctic. *Tellus B: Chemical and Physical Meteorology*, *50*(1), 34–50. https://doi.org/10.3402/tellusb.v50i1.16020

Wilmouth, D. M., Hanisco, T. F., Donahue, N. M., & Anderson, J. G. (1999). Fourier transform ultraviolet spectroscopy of the A 2Π3/2 ← X 2Π3/2 transition of BrO. *The Journal of Physical Chemistry A*, *103*(45), 8935–8945. https://doi.org/10.1021/jp991651o

Yang, X., Blechschmidt, A.-M., Bognar, K., McClure-Begley, A., Morris, S., Petropavlovskikh, I., et al. (2020). Pan-Arctic surface ozone: Modelling vs. measurements. *Atmospheric Chemistry and Physics*, *20*(24), 15937–15967. https://doi.org/10.5194/acp-20-15937-2020

Yang, X., Cox, R. A., Warwick, N. J., Pyle, J. A., Carver, G. D., O'Connor, F. M., & Savage, N. H. (2005). Tropospheric bromine chemistry and its impacts on ozone: A model study. *Journal of Geophysical Research*, *110*(23), 1–18. https://doi.org/10.1029/2005JD006244

Yang, X., Pyle, J. A., Cox, R. A., Theys, N., & Van Roozendael, M. (2010). Snow-sourced bromine and its implications for polar tropospheric ozone. *Atmospheric Chemistry and Physics*, *10*(16), 7763–7773. https://doi.org/10.5194/acp-10-7763-2010

Zhao, X., Strong, K., Adams, C., Schofield, R., Yang, X., Richter, A., et al. (2016). A case study of a transported bromine explosion event in the Canadian high arctic. *Journal of Geophysical Research: Atmospheres*, *121*(1), 457–477. https://doi.org/10.1002/2015JD023711

Zhu, L., Jacob, D. J., Eastham, S. D., Sulprizio, M. P., Wang, X., Sherwen, T., et al. (2019). Effect of sea salt aerosol on tropospheric bromine chemistry. *Atmospheric Chemistry and Physics*, *19*(9), 6497–6507. https://doi.org/10.5194/acp-19-6497-2019